LUNDS
UNIVERSITET

MASTER THESIS

"Fat" Nanobeam-Waveguide Resonator for Suppressing Spectral Diffusion in InGaAs Quantum Dots

---

Author:
Qinda GUO

Supervisor:
Asst.Prof. Tim SCHRÖDER
Prof. Peter LODAHL

A thesis submitted in fulfillment of the requirements
for the degree of Master of Science

in the

Quantum Photonics
Department of Physics

LUND UNIVERSITY

Abstract

Faculty of Science
Department of Physics

Master of Science

"Fat" Nanobeam-Waveguide Resonator for Suppressing Spectral Diffusion in InGaAs Quantum Dots

by Qinda GUO

The coherent coupling of photons to solid state emitters is one of the building blocks for future quantum technology. However, one of the main sources for non-perfect or even strongly reduced coherence of the photons is charge noise which introduces energy shifts during or in between the photon emission events. In particular solid-state emitters in nanostructures suffer from such spectral diffusion as surface charge defects from nanofabrication are often only tens of nanometers away from the emitter.

In this thesis, a novel type of light–matter interface, a GaAs-based nanobeam cavity, has been designed and tested to couple emission from self-assembled InAs quantum dot (QD). A wide nanobeam cavity with a modulated outline has been designed and optimized, which possess a high intrinsic quality factor for the fundamental optical mode (10^5 for 450 nm wide cavity and 6×10^4 for 600 nm wide cavity), and is expected to reduce spectral diffusion of the QD originated from the etched defects. First, a Finite Element (Comsol) simulation was used for the design, and secondly, the fabricated design was tested at room and cryogenic temperatures. When the QD was coupled to the wide nanobeam cavity inside cryostat, a fast decay rate of $19 \pm 2\ ns^{-1}$ is measured, resulting in a lifetime of $\sim$ 52.6 ps. Comparing with the lifetime of QDs in bulk material, the spontaneous emission lifetime, i.e. Purcell factor, is derived to be ~ 36 under a non-resonant excitation scheme.

A lifetime of 52.6 ps corresponds to a lifetime-limited linedwidth of 8.37 GHz. Compared to typical non-Purcell enhanced linewidths of about 200 MHz, a linewidth of 8.37 GHz strongly relaxes the sensitivity to charge noise introduced by the environment. Furthermore, and not tested here, the additional distance to surface charges, possible due to the novel "fat" cavity design, should furthermore reduce the induced spectral diffusion as observed before in non-resonant nanostructures [1, 2].

Acknowledgements

The master project has been carried out between January 2018 and March 2019 at Niels Bohr Institute, University of Copenhagen. This work was conducted in the Quantum Photonics group under the supervision of Assistant professor Tim Schröder and Professor Peter Lodahl.

First of all, I would like to extend my gratitude to the head of the group, Peter Lodahl, who has offered me the incredibly great opportunity for entering in this field and working with a number of academically excellent colleagues. I very much appreciated the instructions from Tim Schröder, who gave me this great project. For so many times I had felt confused and frustrated about the tricky problems that occurred during the year, I was lucky enough to get his inspirational advice and encouraging words, to motivate me keeping forward. In a nutshell, he is not only a great project supervisor but also a superb guide for where I am heading to. I would like to thank Mathieu Gisselbrecht for examining and correcting my thesis at Lund university.

Additionally, I would like to thank all members of the photonics group, who have helped me a lot, especially Xiao-Liu Chu and Nir Rotenberg who helped me with the cryogenic temperature measurement and feedback about the result, and Henri Thyrrestrup for helping me conducting lifetime fitting. I got a lot of inspirations and knowledge from Sandra Madsen who laid a solid base of nanobeam cavity simulation for me to start with, and Zhe Liu and Asli Ugurlu for fabricating the sample and providing the SEM images. I also benefit a lot from the discussion with Leonardo Midolo. Last but not least, I would like to thank everyone (Camille Papon, Dapeng Ding, Xiaoyan Zhou) who read parts of my thesis and gave great comments during the writing process.

Finally, I would like to thank my family for precious and emotional support all the time.

Contents

List of Abbreviations

QKD	**Q**uantum **K**ey **D**istribution
QD	**Q**uantum **D**ot
QED	**Q**uantum **E**lectro- **D**ynamics
SEM	**S**canning **E**lectron **M**icrograph
WL	**W**etting **L**ayer
WLD	**W**etting **L**ayer **D**efects
hh	**h**eavy **h**ole
lh	**l**ight **h**ole
SPS	**S**ingle- **P**hoton **S**ource
BS	**B**eam **S**plitter
LDOS	**L**ocal **D**ensity **O**f **S**tates
PL	**P**hoto- **L**uminescence
FEM	**F**inite **E**lement **M**ethod
PML	**P**erfectly **M**atched **L**ayer
DOS	**D**ensity **O**f **S**tates
TE	**T**ransverse **E**lectric
BEW	**B**and- **E**dge **W**avelength
IPA	**I**so- **P**ropyl **A**lcohol
PEC	**P**roximity **E**ffect **C**orrection
NMP	1-Methyl-2-pyrrolidon
WS	**W**hite-light **S**ource
CCD	**C**harge **C**oupled **D**evice
LP	**L**inear **P**olarizer
PM	**P**ower **M**eter
DF	**D**ensity **F**ilter
FSR	**F**ree **S**pectral **R**ange
APD	**A**valanche **P**hoto- **D**iode
IRF	**I**nstrument **R**esponse **F**unction

Chapter 1

Introduction

The recent years have seen a continuously increasing interest in the field of quantum technologies. The harvesting of the quantum phenomena is at the heart of the investigation. Developing quantum technologies is however highly challenging due to the extremely tiny operation-scale and sensitivity to noise, but are believed to subvert the daily life once achieved. Quantum communication is such an example, within which quantum cryptography enables unconditionally secure communication against eavesdropping. An exciting challenge would be the realization of this quantum communication experiment at space scale [3, 4], which motivates strongly the construction of a quantum network.

In this thesis, we investigate one of the building blocks of such a quantum network, the single-photon source based on solid-state emitters. The most central and appealing application in quantum cryptography is the quantum key distribution (QKD), which is a well-developed scheme for performing cryptography tasks. However, the QKD protocol relies on highly indistinguishable single photons, to perform quantum superposition and entanglement [5]. A highly efficient source of single photons is therefore essential towards this goal. Several schemes for single-photon source are promising, especially the InAs quantum dots (QDs), fluorescent molecules, and defect centres in solid-state materials. In this project, self-assembled InAs QDs are adopted due to the excellent performance, in terms of brightness, single-photon purity, and indistinguishability. Photonic cavities can also be employed to strongly couple and enhance the performance of the embedded QDs. Single photon purity as high as 99% has been reported [6] and indistinguishability over 93% is also achieved [7].

Nevertheless, the challenges for establishing an effective single-photon source based on InAs QDs have not been fully addressed yet. For instance, the cavity QED which describes the light-matter interaction in an inhomogeneous environment has been studied extensively, but experimental realization of strongly coupled system remains challenging. Moreover, for the QD-based single-photon source, the spectral diffusion induced from the etching defects lowers the quality of single photons. The excitation process to quantum dots could cause ionization of trapped charges which mainly gather in the wetting layer defects and etched surfaces. The Coulomb interaction between trapped charges and quantum dots shift the exciton binding energy. This problem can be mitigated by fabricating wider waveguides or nanostructures around, as demonstrated recently [2, 8]. Additionally, placing the single emitter into a cavity can reduce the lifetime of spontaneous emission and meanwhile broaden the natural linewidth. By extending the surrounding area, the broadened profile can be altered from inhomogeneous to homogeneous, resulting in a narrow linewidth. Therefore, in this project, we propose a nanobeam cavity, which has a wide width at the cavity center and is tapered down to a narrow width in the waveguide, to ensure single mode propagating along the waveguide. This modulated outline can keep the QD being far away from any etched surfaces. Such a cavity is designed and optimized by using finite-element method and experimentally tested. It is expected to provide a strong enhancement to the coupled QD and minimize the spectral diffusion.

The thesis is structured into the following chapters:

- Chapter 2: We will introduce the semiconductor quantum dot and its optical properties. Then the mechanism of the nanostructure which acts as an effective interface to couple the single QD will be introduced. The derivation that shows the nanostructure having the ability to modify the density of states around emitter will be given. Finally, we will discuss the spectral diffusion of QD emission induced from the fabrication defects.

- Chapter 3: We will begin with the simulation over a unit cell with a circular hole inside, and then continue to a nanobeam cavity by exploiting the bandedge wavelength of the unit cell. The detailed introduction for the cavity design will be presented.

- Chapter 4: This chapter involves an introduction to the sample fabrication, and the scanning electron micrograph (SEM) pictures are shown.

- Chapter 5: The transmission measurement to the fabricated cavity at room temperature will be presented, and measurement and analysis over 60 different structures will be given.

- Chapter 6: The photoluminescence spectroscopy and lifetime measurement at cryogenic temperature have been performed to investigate the cavity QED, and a coupled QD-cavity system will be shown.

- Chapter 7: A conclusion and outlook of the project will be given.

Chapter 2

Interfacing quantum dots with nanostructures: Theoretical background

This chapter aims to elaborate the relevant theory which has laid a solid foundation for interfacing single QD with nanobeam structure. In particular, the exploration of the interface in this thesis work is limited to GaAs structure with embedded-in self-assembled InAs QD. An introduction to semiconductor QD and its fantastic optical properties are given in section 2.1. Then the nature of photonic nanobeam structure is revealed in section 2.2. The confinement of electromagnetic wave and the origin of the band gap is the focus of this section. Section 2.3 describes the mechanism of interaction underlying QD-cavity coupled system, which is at the heart of this work, proving the controllability of the QD decay. Among them, the spectral diffusion which obstructs the quality of single-photon emission will be discussed.

2.1 Semiconductor quantum dots

Semiconductor quantum dot is an 'artificial atom' which consists typically of $10^4 \sim 10^6$ individual atoms, but its optical properties are similar with single atoms due to to the nano-scale level quantum confinement from heterostructure, as shown in Figure 2.1. This confinement creates discrete electronic states in QD, and the energy level spacing depends on the size of QD. Comparing the QD size to Bohr radius from electron and hole can define the strong-, weak-, intermediate-confinement regime. However, we focus on the strong confinement regime where the energy level spacing is more extensive than Coulomb energy. Thus the model that treats Coulomb effect as perturbation and independently manage the motion of carriers in conduction and valence band can be used. The active optical mechanism for the quantum dot is mainly excitonic at low temperature, while the uncorrelated electron-hole interaction is suppressed. The interaction strength

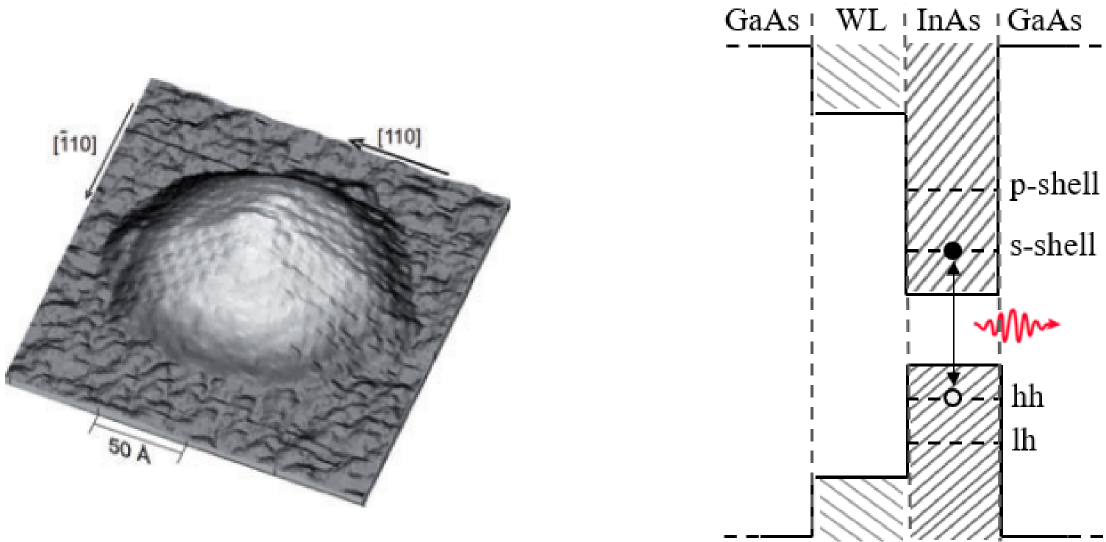

(a)

(b)

FIGURE 2.1: Semiconductor quantum dot. (a). Scanning tunneling micrographs showing the structural property of Stranski-Krastanov quantum dots with a pyramidal shape [9]. (b). Profile of energy bands for the heterostructure. The sandwich-like confinement caused the discrete electronic states in quantum dots. Wetting layer (WL) is an initial layer of atoms that is epitaxially grown on GaAs, upon which the self-assembled InAs QDs are created. The energy levels of the QD are discrete, which are represented by electron shells of s, p in the conduction band, and heavy hole (hh), light hole (lh) in the valence band, for the two lowest levels.

of electron-hole bound state is described by a transition matrix element of the moment between conduction and valence band,

$$\begin{aligned} \boldsymbol{P} &= \langle \Psi_v | \, \boldsymbol{p} \, | \Psi_c \rangle \\ &= \langle F_v | F_c \rangle \, \langle u_v | \, \boldsymbol{p} \, | u_c \rangle_{uc} \, \langle \alpha_v | \alpha_c \rangle \end{aligned} \tag{2.1}$$

where $\boldsymbol{p}$ is the momentum operator, the subscripts v and c represents the quantity from valence band or conduction band, respectively. Ψ is the quantum state for an electron in the conduction band or valence band and is expressed as $\Psi = |F\rangle \, |u\rangle \, |\alpha\rangle$, three notations from left to right are envelope wave function, electronic Bloch function, and the spin state. Equation 2.1 implies the selection rules for optical transition in bound state: i) the envelope functions should be in same parity, ii) Bloch functions should be in opposite parity, iii) the spin states should be same before and after. The electron-hole picture is commonly used to describe the quantized electronic energy states, and for the splits in valence band states, heavy hole owns the lowest energy. Therefore the subscripts of 'v' can be replaced by 'h' referred to the heavy hole. The possible spin states for holes are $|\Uparrow\rangle = |u_c\rangle\,|\uparrow_h\rangle$ and $|\Downarrow\rangle = |u_c\rangle\,|\downarrow_h\rangle$, the electron spin states are $|\uparrow\rangle$ and $|\downarrow\rangle$ with similar expressions.

2.1.1 Decay dynamics

For a neutral exciton which consists of an electron and a heavy hole, the three-level scheme is commonly used to describe the optical properties of the exciton. Figure 2.2 depicts a sketch of the scheme. Due to the exchange interaction, the electronic state in conduction band splits into bright-exciton and dark-exciton [10], and they can be expressed by Bloch sphere vectors, $|X_B\rangle = \frac{1}{\sqrt{2}}(|\Uparrow\downarrow\rangle - |\Downarrow\uparrow\rangle)$, $|X_D\rangle = \frac{1}{\sqrt{2}}(|\Uparrow\uparrow\rangle - |\Downarrow\downarrow\rangle)$. The splitting is normally hundreds μeV. Bright exciton may be transformed to dark exciton by an interband process called spin-flip, in which the necessary energy for the transition is from acoustic phonons [11]. However, the spin-flip rate is much slower than the radiative decay.

Although the dark state does no interact with incident light, if a non-resonant excitation is applied to this neutral system, both states can be populated. The population of the excited state is,

$$N(t) = A_f e^{-\gamma_f t} + A_s e^{-\gamma_s t} \tag{2.2}$$

Two channels are inducing the population to the ground state, through fast and slow decay, as shown by the two terms in Equation 2.2. A_f and A_s are the amplitudes of the fast and slow decay, and γ_f and γ_s are the decay rates of the fast and slow decay, respectively. These four parameters can be expressed as [12],

$$\begin{cases} A_f = N(0)(1+\frac{\gamma^B_{rad}}{\gamma_f-\gamma_s})/2 - N(0)\frac{\gamma_{sf}}{\gamma_f-\gamma_s} \\ A_s = N(0)(1-\frac{\gamma^B_{rad}}{\gamma_f-\gamma_s})/2 + N(0)\frac{\gamma_{sf}}{\gamma_f-\gamma_s} \\ \gamma_f = \gamma^B_{rad}/2 + \gamma^B_{nrad} + \gamma_{sf} + \sqrt{(\gamma^B_{rad}/2)^2 + \gamma^2_{sf}} \\ \gamma_s = \gamma^B_{rad}/2 + \gamma^B_{nrad} + \gamma_{sf} - \sqrt{(\gamma^B_{rad}/2)^2 + \gamma^2_{sf}} \end{cases} \tag{2.3}$$

where γ^B_{rad} and γ^B_{nrad} are the radiative decay rate and non-radiative decay rate of bright exciton, respectively. γ_{sf} is the spin-flip rate between bright and dark excitons. The existence of fast and slow decay mechanism renders the decay profile to be bi-exponential, as a comparison, the biexcitons or trions which have no energy splitting follows a single-exponential decay.

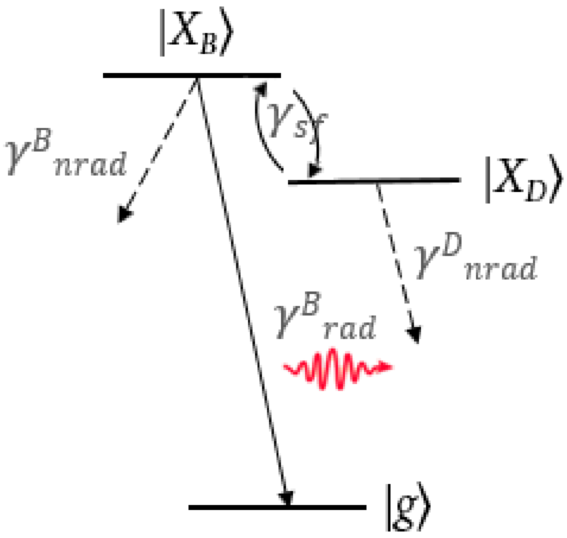

FIGURE 2.2: The simple three-level optical transition scheme for neutral exciton. $|X_B\rangle$ and $|X_D\rangle$ are the bright and dark states of exciton excited states, the transition between them is possible via spin-flip process with a rate of γ_{sf}. γ^B_{nrad} and γ^D_{nrad} are the non-radiative decay from bright state and dark state, respectively. γ^B_{rad} is the fast decay rate for the radiative recombination by emitting one photon.

2.1.2 Coherence for single-photon emission

Single-photon emission is at the heart of the properties of self-assembled quantum dots. It is crucial for the application in quantum communication and simulator for the single-photon source (SPS). The single-photon emission is the light source that only emits one photon during a specific time range. The single photon emission is feasible for self-assembled quantum dot due to the discrete and far apart energy levels, such that the majority of the optical transitions occurrs in single exciton, even under non-resonant excitation scheme. The process of multi-photon emission, therefore, should be suppressed to minimize the mix up with identical photons and thus improve the 'quality' of single photon emission. The 'quality' for an SPS can be classified as three aspects which comprised important characteristics of SPS: single photon purity, indistinguishability and brightness.

The single-photon purity is the probability of emitting a single photon, so ideally the purity should be unity. In photon statistics, the purity can be quantified by recording the second-order correlation function which is defined as,

$$g^{(2)}(0) = \frac{\langle n_1(t)n_2(t)\rangle_t}{\langle n_1(t)\rangle_t \langle n_2(t)\rangle_t} \tag{2.4}$$

where $n_i(t)$ is the probed number of counts for the desired mode at time t. For the probed ensembles of light, it can be decomposed into quantized harmonics with different modes, which are defined by spatial wave vector $\boldsymbol{k}$ and polarization p [13]. The photon wavepacket is,

$$|\psi\rangle = \sum_{\boldsymbol{k},p,n} c_{\boldsymbol{k},p} |n\rangle_{\boldsymbol{k},p} \tag{2.5}$$

$|n\rangle_{\boldsymbol{k},p}$ is the Fock state indicating the pure state and its number of photons. The single-photon Fock state is $|1\rangle_{\boldsymbol{k},p}$, with 1 photon in total. $g^{(2)}(0)$ can be calculated with $g^{(2)}(0) = 1 - 1/n$ based on Fock state, therefore $g^{(2)}(0) = 0$ for an ideal SPS. The highly pure single photon emission is required for SPS in the application of quantum communication and quantum computation, to ensure the absolutely security [14] and minimize the errors [15, 16, 17].

Indistinguishability means the subsequently emitted photons are identical and indistinguishable. Indistinguishable photons are the essential requirement for building two-photon quantum gates via photon-photon interaction [13]. The Hong-Ou-Mandel effect is commonly used to quantify the indistinguishability [18], which uses a beamsplitter (BS) with two ports collecting photons at the same time and two detectors are placed at each exit of BS. The quantum interference process occurrs if the two photons are in the same pure quantum states. As a result, they go out of the BS together only through one exit and are sensed by one detector.

The single-photon emission should possess a high brightness, which means the spontaneous decay into the radiative component is predominant, with only extremely slight parts are coupled into vacuum or dark state. The brightness of SPS determines the upper limit of scalability of integrated photonic platform [13]. For a cavity-QD coupled system, the Purcell effect can significantly enhance the repetition rates of spontaneous emission, and boost the level of brightness. Moreover, the optimization in the collection efficiency of the system is a way to improve the brightness. However, the brightness at the experimental point of view has no uniform definition, because the operation to measurement can be in different positions (strictly output of grating coupler or detector).

2.2 Photonic crystal nanobeam waveguide

The photonic nanostructure is an effective interface for single-emitter like quantum dots since the modified vacuum fluctuation environment can couple and enhance the QD emission to the desired mode. This ability to support the certain mode is originated from the periodical variation of dielectric permittivity $\epsilon(\boldsymbol{r})$.

The contrast of refractive index provides the optical Bragg scattering to propagation, and the scattering strength is proportional to the degree of contrast.

2.2.1 Electromagnetism in mixed dielectric medium

We start from macroscopic Maxwell equations that is a set derivative functions, describing the relation of electric($\boldsymbol{E}$) or magnetic($\boldsymbol{H}$) field with the charge(ρ) or current($\boldsymbol{J}$) density, to study the light propagation in nanophotonic structure,

$$\begin{aligned} \nabla \cdot \boldsymbol{B} = 0 \qquad & \nabla \times \boldsymbol{E} + \frac{\partial \boldsymbol{B}}{\partial t} = 0 \\ \nabla \cdot \boldsymbol{D} = \rho \qquad & \nabla \times \boldsymbol{H} - \frac{\partial \boldsymbol{D}}{\partial t} = \boldsymbol{J} \end{aligned} \tag{2.6}$$

where $\boldsymbol{B}$ and $\boldsymbol{D}$ are the displacement and magnetic induction fields. Several restrictions and approximations can be applied to the set of equations, making it more suitable for a mixed dielectric environment. We assume the field strength is so weak that the polarization density has a linear respond to electric field, and the material is macroscopic and isotropic, then the $\boldsymbol{B}$ and $\boldsymbol{D}$ can be expressed by electric and magnetic field as, $\boldsymbol{D}(\boldsymbol{r}) = \epsilon_0 \epsilon(\boldsymbol{r}) \boldsymbol{E}(\boldsymbol{r})$ and $\boldsymbol{B}(\boldsymbol{r}) = \mu_0 \mu(\boldsymbol{r}) \boldsymbol{H}(\boldsymbol{r})$, where ϵ_0 and ϵ are the vacuum and relative permittivity, μ_0 and μ are the vacuum and relative permeability, respectively. But the relative permeability is so close to unity that can be neglected in many cases, therefore the refractive index can be expressed as the square root of relative permittivity, $n = \sqrt{\epsilon \mu} = \sqrt{\epsilon}$. The Maxwell equations with these approximations are,

$$\begin{aligned} \nabla \cdot \boldsymbol{H}(\boldsymbol{r}, t) = 0 \qquad & \nabla \times \boldsymbol{E}(\boldsymbol{r}, t) + \mu_0 \frac{\partial \boldsymbol{H}(\boldsymbol{r}, t)}{\partial t} = 0 \\ \nabla \cdot [\epsilon(\boldsymbol{r}) \boldsymbol{E}(\boldsymbol{r}, t)] = 0 \qquad & \nabla \times \boldsymbol{H}(\boldsymbol{r}, t) - \epsilon_0 \epsilon_(\boldsymbol{r}) \frac{\partial \boldsymbol{E}(\boldsymbol{r}, t)}{\partial t} = 0 \end{aligned} \tag{2.7}$$

the $\boldsymbol{E}$ and $\boldsymbol{H}$ are both time- and spatial- dependent, and can be decomposed into harmonic modes,

$$\begin{aligned} \boldsymbol{H}(\boldsymbol{r}, t) &= \boldsymbol{H}(\boldsymbol{r}) e^{-i\omega t} \\ \boldsymbol{E}(\boldsymbol{r}, t) &= \boldsymbol{E}(\boldsymbol{r}) e^{-i\omega t} \end{aligned} \tag{2.8}$$

where $\boldsymbol{H}(\boldsymbol{r})$ and $\boldsymbol{E}(\boldsymbol{r})$ represent the spatial mode profile, and the exponential term indicates the time evolution of harmonic modes. By doing some mathematical derivations [19], one can get,

$$\nabla \times (\frac{1}{\epsilon(\boldsymbol{r})} \nabla \times \boldsymbol{H}(\boldsymbol{r})) = (\frac{\omega}{c})^2 \boldsymbol{H}(\boldsymbol{r}) \tag{2.9}$$

This is referred to as the master equation, which will be used to calculate the electromagnetic mode profile for any given dielectric material with relative permittivity $\epsilon(\boldsymbol{r})$. The derivations for the mixed dielectric material mean that the solving-harmonic modes is an eigenvalue problem, that is, the result should be a set of eigenfunctions and the corresponding eigenvalues. Thus ω^2/c^2 is the eigenvalue for a set of harmonic modes where ω is the angular frequency of modes.

2.2.2 Electromagnetism in periodic dielectric medium

We consider a one-dimensional photonic crystal that has periodically varying dielectric constant in the y-direction, but unchanged along x and z-direction. This variation in y-direction has a minimum period a, satisfying $\epsilon(\boldsymbol{y}) = \epsilon(\boldsymbol{y} + \boldsymbol{a})$. This basic step length a is called lattice constant, and the periodicity in the y-direction is referred to as discrete translational symmetry. The periodically changing dielectric constant indicates that the solution of spatial mode profile from Equation 2.9 should also be periodic, and this can be achieved by multiplying the plane wave of free space and a periodic function $u_k(y)$ [20],

$$H_k(y) = u_k(y)e^{iky}, \qquad u_k(y+a) = u_k(y) \tag{2.10}$$

where k is the Bloch wave number. This equation is referred to as the *Bloch's theorem* for the wavefunction in crystal. $u_k(y)$ is the periodic envelop function, and it should satisfy [21]

$$(\nabla + ik) \times \frac{1}{\epsilon}(\nabla + ik) \times u_k(y) = (\frac{\omega(k)}{c})^2 u_k(y) \tag{2.11}$$

For any value of k that lies in the range $m \cdot \pi/a < k < (m+2) \cdot \pi/a$ (m is an odd number), the wavefunction is always in a fixed form,

$$\begin{aligned} H_k(y) &= u_k(y)e^{iky} \\ &= u_k(y)e^{iy(k'+(m+1)(2\pi/a))} \\ &= [u_k(y)e^{(m+1)\cdot 2\pi iy/a}]e^{ik'y} \\ &= u'_k(y)e^{ik'y} \end{aligned} \tag{2.12}$$

where $|k'| < \pi/a$, is called the first Brillouin zone. u'_k is an envelop function with the same periodic length a as u_k.

2.2.3 Photonic band structure

Thin lines in Figure 2.3 show the dispersion relation for free electrons, expressed by $E_0(k) = \hbar^2 k^2/(2m_0)$. However, in a periodic structure, the free-electron parabola tends to be flat at both lower and upper levels, when k is close to zone boundaries. As derived in Section 2.2.2, the Bloch wave number k can be reduced to the first Brillouin zone, while the wavefunction is unchanged. The reduced zone scheme is shown in Figure. 2.3 (b), and a band gap is formed between two levels, where there is no density of states and therefore no propagation is allowed.

The origin of the band gap can be explained by Bragg reflection theory, and the detailed explanation can be found in [20]. Briefly, a wave that is propagating along the periodic structure, such as photonic crystal, can be scattered by the lattice. However, the scattering is particularly strong at the Bragg condition,

$$n\lambda = 2asin\theta \tag{2.13}$$

where $\lambda = 2\pi/k$. The angle θ of the incident wave onto the planes of the crystal can take $\pi/2$ if we assume the wave normally travels to the plane. Hence the Bragg condition becomes $k = n\pi/a$. Once the condition is fulfilled, the backscattering will be very strong, and the incident electrons become a standing wave.

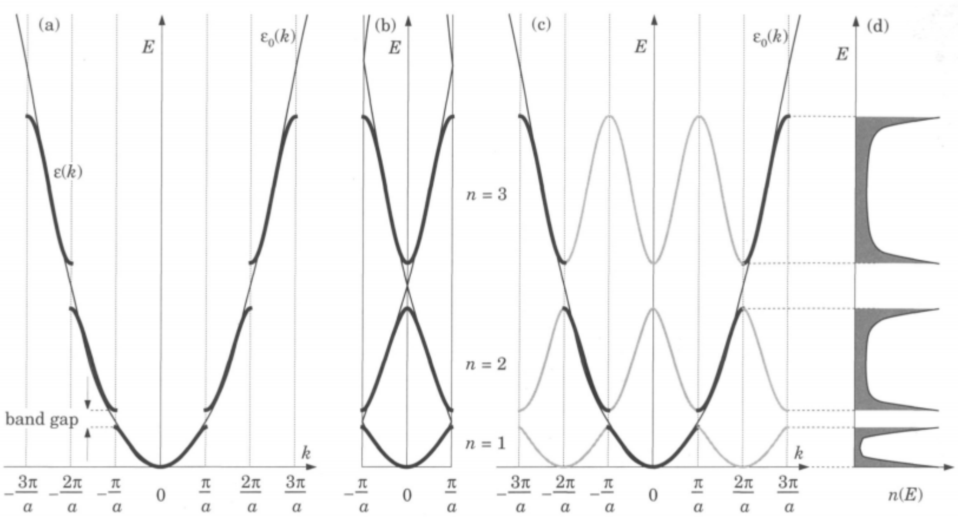

FIGURE 2.3: The band structure for one dimensioanl photonic crystal. (a), (b) and (c) shows the extended, reduced and repeated zone schemes as a function of energy, respectively. (d) shows the density of states as a function of energy. Grey line indicates the periodic repetition, thick and thin lines indicates $E(k)$ in a periodic structure or free space, respectively. Figure courtesy [20].

2.3 Coupling single QD with nanobeam structure

2.3.1 Spontaneous emission of single photons in homogeneous environment

In this section, the spontaneous decay for an emitter in free space is derivated, and the Weisskopf-Wigner approximation is used. We consider a simple two-level dipole system with transition frequency ω_0 between the ground state $|0\rangle$ and the excited state $|1\rangle$, the coupling to continuum could be optical mode at frequency $\omega_{\boldsymbol{k}}$ with any possible vector $\boldsymbol{k}$. We start from a Hamiltonian with the form

$$\begin{aligned} \hat{H}_{tot} &= \hat{H}_{atom} + \hat{H}_{vacuum} + \hat{H}_{int} \\ &= \frac{1}{2}\hbar\omega_0\hat{\sigma}_z + \sum_k \hbar\omega \hat{a}_k^+ \hat{a}_k + \hbar\sum_k (g_k \hat{\sigma}^+ a_k + h.c.) \end{aligned} \tag{2.14}$$

where $\hat{a}_k$ and $\hat{a}_k^+$ are annihilation and creation operators for photons at $\boldsymbol{k}$ mode, respectively. g is the interaction strength of the single emitter with mode $\boldsymbol{k}$.

The general state vector for the coupled system is,

$$|\psi(t)\rangle = c_e(t)e^{-i\omega_0 t}\,|e,0\rangle + \sum_k c_{gk}(t)e^{-i\omega_k t}\,|g,l_k\rangle\,, \tag{2.15}$$

where the summation is taken over all the possible modes. $c_e(t)$ is the time-dependent probability for the excited two-level system and zero photon state and $c_{gk}(t)$ is the time-dependent probability for the two-level system in its ground state and a photon at mode $\boldsymbol{k}$. Inserting this state vector and the Hamiltonian (Equation 2.14) into the time-dependent Schrödinger equation, the equations of motion for the excited and ground states can be expressed as,

$$\begin{cases} \dot{c}_e(t) = -i\sum_k g_k e^{-i(\omega_k-\omega_0)t} c_{gk}(t) \\ \dot{c}_{gk}(t) = -ig_k^{\star} e^{i(\omega_k-\omega_0)t} c_e(t) \end{cases} \tag{2.16}$$

Integrating $\dot{c}_{gk}(t)$ and inserting the result into the expression of $\dot{c}_e(t)$, one can get,

$$\begin{aligned} \dot{c}_e(t) = &-\sum_k |g_{\boldsymbol{k}}(\boldsymbol{r_0})|^2 \int_0^t dt' c_e(t') e^{-i(\omega_k-\omega_0)(t-t')} \\ &- i\sum_k g_{\boldsymbol{k}}^{\star}(\boldsymbol{r_0}) c_{g,k}(0) e^{(-i\omega_k-\omega_0)t} \end{aligned} \tag{2.17}$$

We now consider the situation of spontaneous emission with the two-level system initially in the excited state, i.e. $c_e(0) = 1$ and $c_{g,k}(0) = 0$. Therefore, the last term of Equation 2.17 can be omitted. In vacuum, the summation over all of the discrete mode $\boldsymbol{k}$ can be converted to [22],

$$\sum_k \longrightarrow 2\frac{V}{(2\pi)^3}\int_0^{2\pi} d\phi \int_0^{\pi} d\theta sin\theta \int_0^{\infty} dkk^2, \tag{2.18}$$

where the factor of 2 accounts for the two orthogonal polarizations. Combining with $g_k(\boldsymbol{r_0}) = i\boldsymbol{\mu}\cdot \boldsymbol{E}_k^\star(r0)/\hbar$, where μ is the transition dipole moment and $\boldsymbol{E}_k^\star(r0)$ is the electric field at position $\boldsymbol{r_o}$, Equation 2.17 without last term changes to,

$$\dot{c}_e(t) = -\frac{\mu^2}{6\pi^2\epsilon_0\hbar c^3}\int_0^{\infty}\omega_k^3\int_0^t c_e(t')e^{-i(\omega_k-\omega_0)(t-t')}dt'd\omega_k \tag{2.19}$$

The Weisskopf-Wigner approximation [23] is introduced here to simplify further.

$$\dot{c}_e(t) = -\frac{\mu^2}{6\pi^2\epsilon_0\hbar c^3}c_e(t)\int_0^{\infty}\omega_k^3\int_0^t e^{-i(\omega_k-\omega_0)(t-t')}dt'd\omega_k \tag{2.20}$$

The equation of motion of the excited state covers the information about decay constant to free space and the Lamb shift,

$$\dot{c}_e(t) = -(\frac{\gamma_0}{2} + i\delta\omega)c_e(t) \tag{2.21}$$

where the imaginary term indicates the Lamb shift and the γ_0 is the free space decay constant,

$$\begin{aligned}\gamma_0 =& \frac{\omega_0^3\mu^2}{3\pi n\hbar c^3}\\ =& \frac{\omega_0\mu^2\pi}{3n\hbar}\rho_{(\omega_0)}\end{aligned} \tag{2.22}$$

where $\rho_{(\omega_0)} = \omega_0^2/(\pi^2c^3)$ is the local-density-of-states(LDOS), which indicates the number of electromagnetic modes that a photon can occupy. So far the spontaneous decay constant in homogeneous environment has been derived, and the result implies the decay rate is directly controlled by LDOS, the modification to LDOS enables an enhancement to spontaneous emission [24].

2.3.2 Spontaneous emission of single photons in inhomogeneous environment

To investigate the QED in inhomogeneous environment which is charaterized by lossless dielectric constant $\epsilon_{(}r)$, we start from canonical Hamiltonian,

$$\hat{H} = \hbar\omega_x \hat{\sigma}_x^+ \hat{\sigma}_x^- + \sum_k \hbar\omega_k \hat{a}_k^\dagger \hat{a}_k - i\hbar \sum_k (\hat{\sigma}_x^- + \hat{\sigma}_x^+)(g_k \hat{a}_k - g_k^\star \hat{a}_k^\dagger) \tag{2.23}$$

where $\hat{\sigma}_x^{+/-}$ represents the Pauli operators of QD exciton. g_k is the coupling strength and can be expressed as $g_k(\boldsymbol{r}) = \sqrt{\frac{\omega_k}{2\hbar\epsilon_0}} \boldsymbol{\mu} \boldsymbol{u_k}(\boldsymbol{r})$. $\boldsymbol{u}_k(\boldsymbol{r})$ are eigenmode profiles of the dielectric structure and can be used as basis for the electromagnetic field such as,

$$\hat{\boldsymbol{E}}(\boldsymbol{r}, t) = \sum_k [\sqrt{\frac{\hbar\omega_k}{2\epsilon_0}} \boldsymbol{u_k}(\boldsymbol{r}) \hat{a}_k e^{-i\omega_k t} + h.c.] \tag{2.24}$$

The Heisenberg equations of motion,$\dot{A}_H(t) = (1/(i\hbar))[A_H(t), H]$,are applied to Equation 2.23 to derive the operators,

$$\begin{cases} \frac{d\hat{a}_k}{dt} = g_k^\star(\hat{\sigma}_x^- + \hat{\sigma}_x^+) - i\omega_k \hat{a}_k \\ \frac{d\hat{a}_k^\dagger}{dt} = g_k(\hat{\sigma}_x^- + \hat{\sigma}_x^+) + i\omega_k \hat{a}_k^\dagger \\ \frac{d\hat{\sigma}_x^-}{dt} = -\sum_k (g_k \hat{a}_k - g_k \hat{a}_k^\dagger) - i\omega_0 \hat{\sigma}_x^- \\ \frac{d\hat{\sigma}_x^+}{dt} = \sum_k (g_k \hat{a}_k - g_k \hat{a}_k^\dagger) + i\omega_0 \hat{\sigma}_x^+, \end{cases} \tag{2.25}$$

this set of equations can be performed with a Laplace transform and inserted into Equation 2.24, to derive the exact electric-field operator.

To describe the electric field in photonic medium, the Green's tensor $\overleftrightarrow{G}(\boldsymbol{r}, \boldsymbol{r'}; \omega)$ is a very useful expression which describes the field response at position $\boldsymbol{r}$ from an oscillating dipole source at position $\boldsymbol{r'}$. It is defined from,

$$\nabla \times \nabla \times \overleftrightarrow{G}(\boldsymbol{r}, \boldsymbol{r'}; \omega) - \frac{\omega^2}{c^2} \epsilon(r) \overleftrightarrow{G}(\boldsymbol{r}, \boldsymbol{r'}; \omega) = \frac{\omega^2}{c^2} \overleftrightarrow{I} \delta(\boldsymbol{r} - \boldsymbol{r'}) \tag{2.26}$$

The Green's function can be expanded in mode functions as [12],

$$\overleftrightarrow{G}(\boldsymbol{r}, \boldsymbol{r'}; \omega) = \sum_k \omega^2 \frac{\boldsymbol{u}_k(\boldsymbol{r}) \otimes \boldsymbol{u}_k^\star(\boldsymbol{r'})}{\omega_k^2 - \omega^2} \tag{2.27}$$

Considering a QD exciton in vacuum field, the electric field operator is [25]

$$\hat{\boldsymbol{E}}(\boldsymbol{r},\omega) = \frac{\overleftrightarrow{G}(\boldsymbol{r},\boldsymbol{r'};\omega)\cdot\hat{\boldsymbol{p}}(\omega)}{1-\boldsymbol{n}_d\cdot\overleftrightarrow{G}(\boldsymbol{r},\boldsymbol{r'};\omega)\cdot\boldsymbol{n}_d\alpha_0(\omega)} \tag{2.28}$$

where $\hat{\boldsymbol{p}}(\omega)$ represents a quantum dipole source and $\alpha_0(\omega)$ is the bare polarizability, they can be expressed as,

$$\hat{\boldsymbol{p}}(\omega) = \hat{\boldsymbol{p}}[\hat{\sigma}_+(\omega)+\hat{\sigma}_-(\omega)] \tag{2.29}$$

$$\alpha_0(\omega) = \frac{2\omega_0\mu^2}{(\hbar\epsilon_0)(\omega_0^2-\omega^2)} \tag{2.30}$$

Expand the quantum field operator based on these two expressions and rearrange, one can get,

$$\hat{\boldsymbol{E}}(\boldsymbol{r},\omega) = \overleftrightarrow{G}(\boldsymbol{r},\boldsymbol{r'};\omega)\frac{[\hat{\sigma}_+(\omega)(\omega+\omega_0)^2+\hat{\sigma}_-(\omega)(\omega-\omega_0)^2]}{\omega_0^2-\omega-i\omega\gamma} \tag{2.31}$$

where $i\omega\Gamma(\boldsymbol{r},\omega)$ is the self-energy term, It contains the information about spontaneous emission rate, which is,

$$\gamma(\boldsymbol{r},\omega) = \frac{2\mu^2}{\hbar\epsilon_0}\boldsymbol{n}_d\cdot Im[\overleftrightarrow{G}(\boldsymbol{r},\boldsymbol{r'};\omega)]\cdot\boldsymbol{n}_d \tag{2.32}$$

so the Purcell factor is obtained by the definition that the ratio of decay rate in actual environment, to the decay rate in a homogeneous medium, since the spontaneous decay constant is proportional to LDOS,

$$F_P(\boldsymbol{r},\omega) = \frac{\boldsymbol{n}_d\cdot Im[\overleftrightarrow{G}(\boldsymbol{r},\boldsymbol{r'};\omega)]\cdot\boldsymbol{n}_d}{\boldsymbol{n}_d\cdot Im[\overleftrightarrow{G}_{hom}(\boldsymbol{r},\boldsymbol{r'};\omega)]\cdot\boldsymbol{n}_d} \tag{2.33}$$

where $\boldsymbol{n}_d\cdot Im[\overleftrightarrow{G}_{hom}(\boldsymbol{r},\boldsymbol{r'};\omega)]\cdot\boldsymbol{n}_d = n\omega^3/(6\pi c^3)$, this can be derived from the result of decay rate in homogeneous environment.

2.3.3 Purcell factor derivation in a photonic nanocavity

The expression for Purcell factor can be derived further, until a more practical form combined with the spatial mismatch term, spectral mismatch term and the term of optimal factor with positioned source. It will also involve the ratio of

Q/V, implying the influence from cavity performance and mode profile applied to Purcell enhancement.

The Green tensor can be expressed with LDOS, by using Equation 2.27 [12],

$$\boldsymbol{n}_d \cdot Im[\overleftrightarrow{G}(\boldsymbol{r},\boldsymbol{r'};\omega)] \cdot \boldsymbol{n}_d = \frac{\pi\omega}{2}\rho(\boldsymbol{r},\omega) \tag{2.34}$$

Substitute it with Equation 2.32, one can get,

$$\gamma(\boldsymbol{r},\omega) = \frac{\pi\omega_0\mu^2}{\epsilon_0\hbar}\rho(\boldsymbol{r},\omega) \tag{2.35}$$

So now the Purcell factor is,

$$\begin{aligned} F_P(\boldsymbol{r},\omega) &= \frac{\gamma(\boldsymbol{r},\omega)}{\gamma_0} \\ &= \frac{3\pi^2c^3}{n\omega^2}\rho(\boldsymbol{r},\omega) \end{aligned} \tag{2.36}$$

In most cases, the nanobeam cavity supports single transverse non-degenerate mode. Based on this assumption, the Green tensor of Equation 2.27 can be written as [25],

$$\overleftrightarrow{G}(\boldsymbol{r},\boldsymbol{r'};\omega) = \omega^2\frac{\boldsymbol{u}_k(\boldsymbol{r})\otimes\boldsymbol{u}_k^{\star}(\boldsymbol{r'})}{\omega_0^2-\omega^2-i\omega\Gamma_0} \tag{2.37}$$

where Γ_0 is the linewidth of cavity resonance profile, $\Gamma_0 = \omega_0/Q$. Combined with Equation 2.36, it leads to a new form of LDOS,

$$\rho(\boldsymbol{r},\omega) = \frac{2}{\pi}\frac{\omega^2\Gamma_0}{(\omega_0^2-\omega^2)^2+\omega^2\Gamma_0^2}|\boldsymbol{u}_k(\boldsymbol{r})|^2|\hat{\boldsymbol{e}}_d\cdot\hat{\boldsymbol{e}}_c|^2 \tag{2.38}$$

Substitute the LDOS with the expression in Equation 2.36, and introduce the expression for effective mode volume $V_{eff} = \int_V \epsilon(\boldsymbol{r})|\boldsymbol{u}_k(\boldsymbol{r})|^2 d^3\boldsymbol{r}/max[\epsilon(\boldsymbol{r})|\boldsymbol{u}_k(\boldsymbol{r})|^2]$. After some rearrangements, one can get,

$$\begin{aligned} F_P^{cav}(\boldsymbol{r},\Delta) &= \frac{3}{4\pi^2}(\frac{\lambda}{n})^3\frac{Q}{V_{eff}}\cdot\frac{\omega_0^2}{\Delta^2\cdot 4Q^2+\omega_0^2}\cdot\frac{\epsilon(\boldsymbol{r})\boldsymbol{u}_k(\boldsymbol{r})|^2|\hat{\boldsymbol{e}}_d\cdot\hat{\boldsymbol{e}}_c|^2}{max[\epsilon(\boldsymbol{r})|\boldsymbol{u}_k(\boldsymbol{r})|^2]} \\ &= F_P^{max}\cdot\delta_f\cdot\delta_x \end{aligned} \tag{2.39}$$

where F_P^{max} is the optimal Pucell factor with positioned source, δ_f defines the spectral mismatch and δ_x defines the spatial mismatch, especially, $|\hat{\boldsymbol{e}}_d\cdot\hat{\boldsymbol{e}}_c|^2$ indicates the mismatch of dipole oscillating direction between emitter and cavity mode.

2.3.4 Spectral diffusion

As shown previously, the solid-state cavity QED can further enhance the application of self-ensembled QD as a very promising on-chip SPS. However, the unavoidable interactions between QD and its adjacent solid-state environment broadened the photoluminescence (PL) spectra, leading to a linewidth usually much broader than the transform-limited value. On the other hand, the transform-limited linewidth is a crucial requirement for quantum key distribution or quantum repeater, that the applications need frequency-locked photon source as essential elements [26]. Thus the understanding and overcome the environmental fluctuation entangled with QDs are required.

The broadening of linewidth is commonly ascribed to spectral diffusion, which modulates the optical transition energy randomly due to the fluctuation of the local electric field in the vicinity of QDs [27, 28, 29, 30]. The fluctuations originate from the randomly trapping or untrapping of charges due to the defect of material. For a nanobeam structure with embedded self-assembled QDs, the defect in the highly disordered wetting layer is one of the main contributions for trapping charges [31]. Nonetheless, spectral wandering induced by the wetting layer defects (WLD) is predominant only under above-band excitation, via the ionization of excitons close to QDs, which is closely related to the power of excitation. At deficient power of above-band-gap excitation, the mechanism of WLD contributes negligible spectral diffusion [32]. Another governing source of trapping charges is the defect provided by rough etched surfaces [33]. The trapped charges create a d.c. Stark effect to the emitter, modulating the transition energy. For the nanobeam cavity, this mechanism provides more significant charge trap and dipole fluctuation, since the QDs usually are very close to the hole surfaces or bulk edges. Both the defects in the wetting layer and etched surfaces show a dependence on the excitation scheme, such that the lower strength of above-band excitation causes less spectral diffusion. One possible solution for solving the problem is by conducting resonance fluorescence on QDs, and together with an additional weak above-band excitation [34], the photogenerated carriers may fill up the traps on etched surfaces to lessen the spectral diffusion. In addition, a PIN diode structure with embedded QDs is also an effective solution to this problem [35].

The QD lineshape should be characterized to investigate and model the effect of spectral diffusion. In the linear response regime, it is determined by QD susceptibility [36],

$$\chi(t) \propto \hat{f}[e^{(i\omega_0-\Gamma_0/2)t}\langle e^{-i\int_0^t d\tau\delta\omega(\tau)}\rangle] \tag{2.40}$$

where $\hat{f}$ denotes the Fourier transform, ω_0 is the resonance frequency of QD and Γ_0 is the radiative linewidth. The statistical average is an integration over all possible frequencies within time τ, and it indicates the underlying probability distribution of the environment. Thus this term reflects the spectral diffusion due to a randomly varying environment. In the case of Gaussian profile fluctuation and exponential correlation function, the statistical average can be expressed as [34],

$$\langle e^{-i\int_0^t d\tau\delta\omega(\tau)}\rangle = e^{-\Phi(t)} \tag{2.41}$$

with

$$\Phi(t) = s^2\tau_c^2[e^{-t/\tau_c} + \frac{t}{\tau_c} - 1] \tag{2.42}$$

where s is the standard deviation of the correlation function and τ_c is the correlation time. Assuming a long time measurement, the broadened linewidth for QDs is a combination of natural QD linewidth with a Lorentzian shape Γ_0 and the contribution from fluctuating environment $s^2\tau_c$, the broadened linewidth is then $\Gamma_0 + s^2\tau_c$, This characterized model for the effect of spectral diffusion provides a way to investigate the broadening in the experiment quantitatively.

Chapter 3

Numerical Modelling of Nanobeam Cavity

In order to explore and investigate the cavity QED with a single emitter, a cavity with strong confinement of optical modes is required. The cavity has the ability to modify the spontaneous emission rate of the quantum emitter. This chapter aims to elaborate on deterministic design for photonic nanobeam cavity with high performance. Section 3.1 briefly introduces the FEM method used in the modelling of the nanobeam cavity. In section 3.2, the unit cell of a nanobeam photonic crystal waveguide is simulated to design a properly located photonic bandgap. In section 3.3, a cavity with ultra-high quality factor can be constructed by utilizing and modulating the bandgap. Then, the wide cavity aiming to provide a more friendly environment to the single emitter is designed and optimized in section 3.4. A more friendly environment implies a larger distance between the emitter and neighboring air-semiconductor interface, to minimize the spectral diffusion by weakening the Stark shift from dopants.

3.1 The finite-element method (FEM)

A frequency-domain finite-element method(FEM) with a perfectly matched layer (PML) is adopted to model the nanobeam photonic cavity. The PML is crucial for correct calculation of the mode volume, which should absorb all the outgoing electromagnetic waves to simulate an open area. Between the cavity structure and PML, buffer layers are applied to suppress the evanescent waves going into PML, and the thickness of the buffer layer follows the λ/n rule [37]. Compared to the time domain simulation, the frequency domain method is much more effective for extracting quality factor of an electromagnetic mode in a cavity. The eigenmode equation in the frequency-domain FEM is,

$$\sqrt{\frac{1}{\mu}}\nabla \times \frac{1}{\epsilon}\nabla \times \sqrt{\frac{1}{\mu}}\tilde{\boldsymbol{H}} = \omega^2\tilde{\boldsymbol{H}} \tag{3.1}$$

which is a combination of Maxwell'equations and second-order differential equation for $\tilde{\boldsymbol{H}} \equiv \sqrt{\mu}\boldsymbol{H}$. The quality factor can be calculated directly from the real and imaginary part of the eigenvalue, which is [37],

$$Q = \frac{Re(\omega)}{2Im(\omega)} \tag{3.2}$$

3.2 Bandstructure calculation from unit cells

A photonic nanobeam cavity consists of many different unit cells, which form a potential well with modified geometric parameters to enhance mode confinement. Therefore, the dispersion relation for each unit cell should be studied, and the corresponding pivotal band gap information should be grasped. The band gap prohibits mode that falls in a certain range of wavelength, resulting in the near zero transmission and near unity reflection. On the other hand, the band edge has a large density of optical states (DOS) and the effect on transmission and reflection is opposite to the band gap. Based on this property, the modulation of band edge wavelength for different unit cells is like building a potential well for propagating mode, is supposed to be a useful tool to construct a photonic resonator.

Figure 3.1 (a) shows the model of a unit cell consisting of nanobeam waveguide and a circular hole from COMSOL, with a lattice constant of 216 nm and a hole radius of 60 nm. The purple color represents the GaAs material waveguide, with a material refractive index of 3.46. Here we only simulate half of the unit cell using symmetry in the structure to save computation power. There is a cut in the bottom surface and alternatively applied with a perfect magnetic conductor to mirror the guided transverse electric (TE) mode considered in our case. Furthermore, the Bloch periodic boundary conditions are put on the slice surface to make the domain infinite on its direction. The size of meshing is set to one-fifth of wavelength inside GaAs material, which ensures a high resolution of the simulation domain and a reliable result

Any periodic dielectric variation in one dimension leads to a bandgap, and small variation leads to small bandgap [21]. The periodicity is set as boundary condition, and parametric sweep for k-vector in the irreducible Brillouin zone from 0 to π/a is conducted. Fourteen eigenfrequencies are searched for in each sweeping step. Figure 3.2 shows the band diagram for the unit cell, with dimensions described in the title of the figure. The dark area represents the light cone and the bands of propagating modes are shown by curves inside the unit cell. The inset plot is the band diagram after the conversion of y-axis to wavelength. For the circular hole unit cell, the 1st-order mode, which is also called dielectric

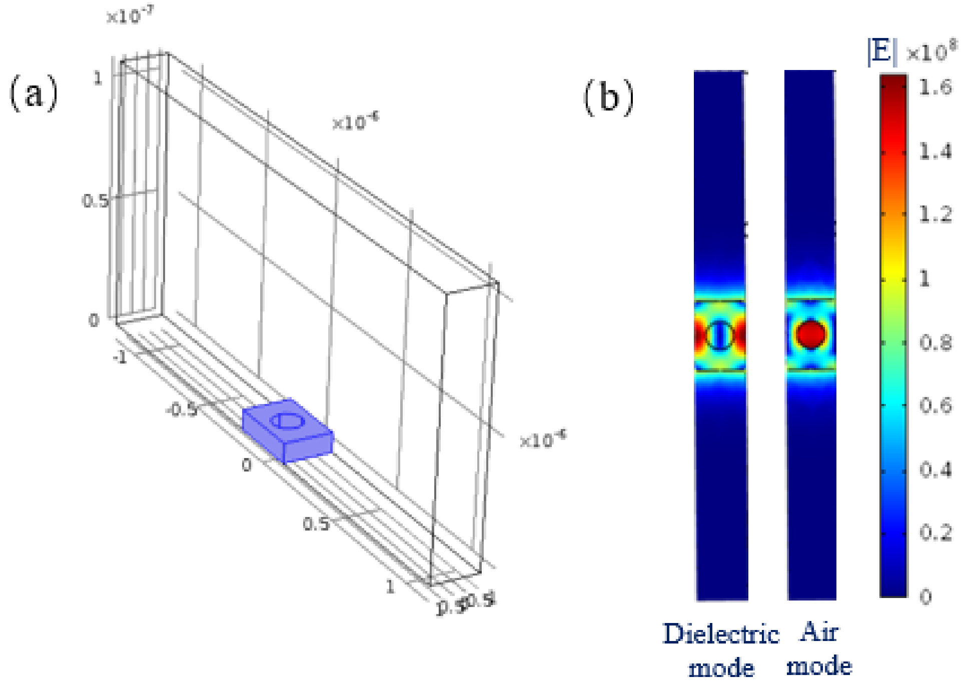

FIGURE 3.1: The model of a unit cell and its mode profiles. (a) The model of half of a unit cell of nanobeam photonic crystal waveguide built up by COMSOL. The purple solid represents the GaAs material, being surrounded by air box. (b) The first one shows the profile of dielectric mode, while the second one exhibits the air mode.

mode, corresponds to an electric field confinement mainly in the dielectric material that is around the center of two circular holes. On the contrary, the 2nd-order mode, air mode, corresponds to an electric distribution mainly inside the hole, as indicated in Figure 3.1 (b). One can use either air mode to construct a downwards potential well by the modulation of the band-edge wavelengths or the dielectric mode but with a reversed well in construction.

3.3 Nanobeam photonic crystal cavity with parabolic potential well

A potential well with the parabolic profile should be constructed to confine the fundamental TE mode, which is normally realized by a parabolic profile modulation to the mirror strength and is effective for a high-quality factor cavity design

[38]. The band-edge wavelength(BEW) of the unit cell at the cavity center determines the wavelength of the fundamental cavity mode, while the difference between the BEW at the most outside hole at cavity to the BEW of the center unit cell determines the potential depth. Therefore, the BEW of the central unitcell should be slightly lower than the QD emission which is assumed to be 930 nm, for the BEW of the outermost unit cell, it is designed to be around 970 nm for appropriate depth of well, as illustrated by inset plot in Figure 3.3 (b). Figure 3.2 shows the band diagram of the outermost unit cell a_5 in the cavity and notably this unit cell also act as mirrors for the cavity, the bandgap is located between 754.3 nm and 972.6 nm, which ideally has a DOS of zero and suppresses the QD emission.

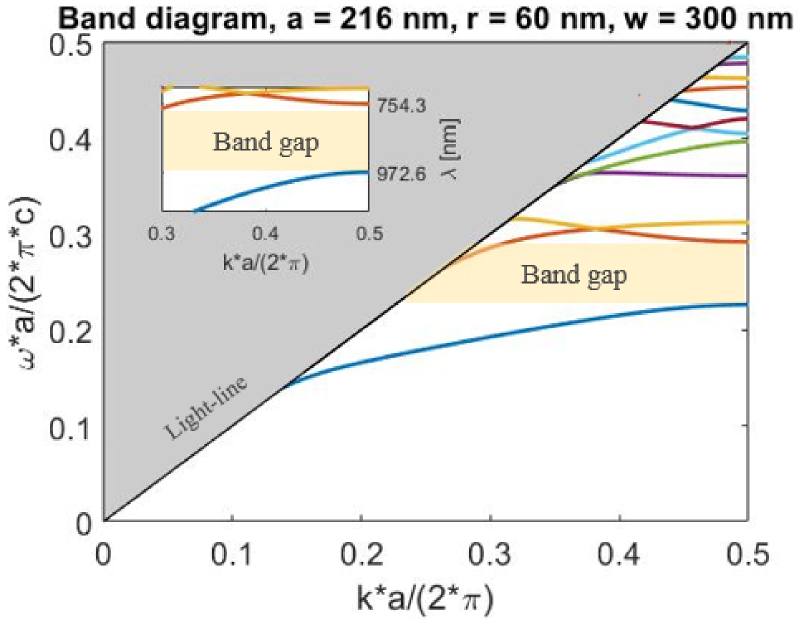

FIGURE 3.2: Band diagram of the circular hole unitcell, with lattice constant of 216 nm, radius of 60 nm and width of 300 nm. The band gap prohibits light propagation between 754.3 nm and 972.6 nm. The grey color area represents the light cone.

TABLE 3.1: The lattice constants with quadratic variation.

Segment	a_0	a_1	a_2	a_3	a_4	a_5	a_{mirror}
Lattice constant [nm]	201	201.6	203.4	206.4	210.6	216	216

The lattice constants follow a quadratic variation from the first hole to last hole in the cavity. For each side of cavity structure, six holes are added in, with lattice constants $a_0, \ldots, a_5$ respectively. According to the pre-set BEW of first and last holes, the lattice constants of them can be determined, since the BEW strongly depends on the lattice constant. Then by applying a quadratic function to a_0 and a_5, and the set of lattice constants between them can be derived, as shown in Table 3.1. The quadratic varying lattice constants result in the parabolic potential well, as Figure 3.3 (b) depicted. The blue dots are the β^2 corresponding to the unit cell with different lattice constants, and the orange line shows the parabolic fit to it, where $\beta = \omega/c$ is the eigenvalue of the optical modes at the edge of the first Brillouin zone. The quality factor for this cavity is 3415 with 38 holes. In conclusion, we have designed a nanobeam cavity, in which mirror strengths of the holes are modulated by a parabolic profile. In the next section, we will transform the straight nanobeam cavity to the wide cavity by utilizing and optimizing these parameters.

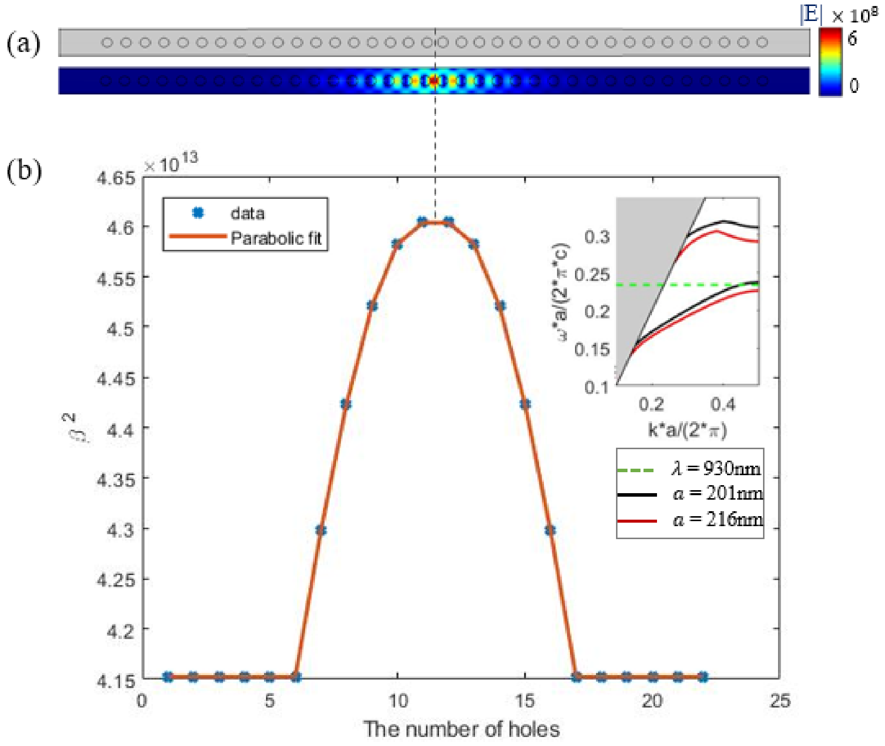

FIGURE 3.3: The cavity design based on the parameters in Table 3.1. (a)The cavity model and also its fundamental mode profile. (b) The β^2 of segments as a function of the unit cell position, which form a parabolic potential well. The inset figure illustrates the band diagram for the first segment a_0 (black) and the last one a_5 (red), the green dashed lines shows the wavelength of 930nm which is assumed to be the QD emission.

3.4 Transformation to the "wide" cavity

3.4.1 The principle of the design

For the design of a nanobeam resonator coupled with a quantum emitter, not only the cavity performance, in terms of quality factor and mode volume, should be taken into account, but also the interaction between the cavity environment and single emitter via Stark effect needs to be considered. The cavity performance largely depends on the construction of the potential well and the geometry of the cavity itself. A more compact structure often results in a cavity with higher performance, for example, a dielectric bowtie photonic crystal structure can provide extremely high Q-factor and ultra-low mode volume at the same time [39]. However, there is often a trade-off between the cavity performance and the spectral diffusion of a quantum emitter sitting inside the cavity. As introduced in Chapter 2, the excitation process to quantum dots could induce ionization of trapped charges which mainly gather in the WLD and etched surfaces. The Coulomb interaction between trapped charges and quantum dots shift the exciton binding energy. Therefore extending the distance between quantum dots and air-semiconductor interface is desirable to minimize the spectral diffusion. Moreover, placing the single emitter into a cavity can reduce the lifetime of spontaneous emission and meanwhile broaden the natural linewidth. By extending the surrounding area, the broadened profile can be altered from inhomogeneous to homogeneous, resulting in a narrow linewidth, Figure 3.4 (a) shows the sketch of the design concept and the profile of the ideal cavity. In short, the center width of the cavity should be stretched, but the waveguide width should be kept constant as 300 nm, to ensure single mode propagating along the waveguide. If the width of waveguide is wider than 300 nm, the waveguide is likely to support higher-order TE modes, which causes the mix coupling of multi-mode. The maximum width at the center of the cavity is designed to be either 450 nm or 600 nm and tapered down to 300 nm with a sinusoidal outline profile. The wider cavity helps keep a linewidth of QD emission closer to transform-limitation. [2, 8].

Following the principles mentioned above, the actual cavity structures with 450 nm and 600 nm width are presented in Figure 3.4 (b) and (c). Compared to the straight cavity in Figure 3.3 (a), the center width is stretched, and taking out two center holes for 450 nm cavity and four holes for 600 nm cavity. For both of the wide cavities, the boundary holes are introduced and located at the intermediate between 1st and 2nd unit cell. Boundary holes are necessary here to significantly enhance the quality factor. The cavity is the part inside the red box, and the blue box shows the nanobeam waveguide together with the region carried mirror holes. The mirror hole is defined as the unit cell that holds a band gap entirely prohibits the resonant mode. The first end holes at both (b) and (c) are an ellipse with 50 nm minor axis and 90 nm major axis, the rest of holes are circles with 60 nm radius.

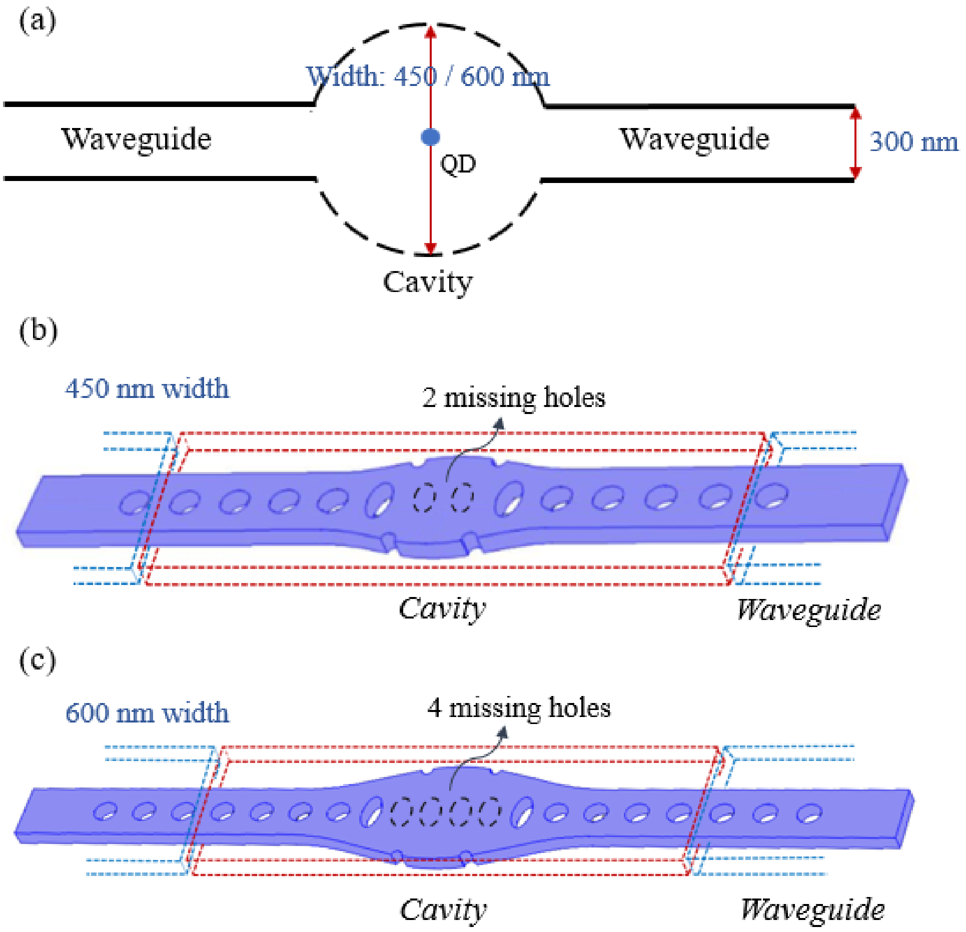

FIGURE 3.4: The concept of a wide cavity, and the actual structure models based the sketch. (a) A sketch shows the concept when designing the wide cavity. (b) and (c) are the completed and optimized structure models in COMSOL for the width of 450nm and 600nm, respectively.

3.4.2 Optimization of lattice constants

The missing of holes and width stretching change the effective refractive index of the unit cells. Therefore a compensation should be made. Generally, changing the width has slight influence to the BEW, due to the plumb between the direction of stretching and the periodic direction of the one-dimensional photonic structure. However, the width of holes should be increased to reduce the scattering loss.

Based on this, the first end holes are modified to be like ellipse. In addition, the lattice constants are crucial for BEW and should be optimized further, to compensate for the changing of effective refractive index.

Instead of only moving the position of holes around to optimize the confinement of photonic cavity and that has been adopted a lot [40, 41], both the hole position and the cavity size are optimized here. Either doing the optimization over the position of holes or lattice constants, the principles are same, which are the re-modulation of effective refractive index. Typically, for an three defect-long (L3) cavity optimization [41], the displacement of holes not only narrow or extend the unit cell of the individual holes, but also change size of the cavity. However, the position of the holes and the size of the cavity are both crucial parameters that determine the cavity performance [42]. Therefore, the optimization based on lattice constants, as indicated in Figure 3.5, is adopted here to treat the unit cell with a hole and bulk material independently, to look for the best combination of them.

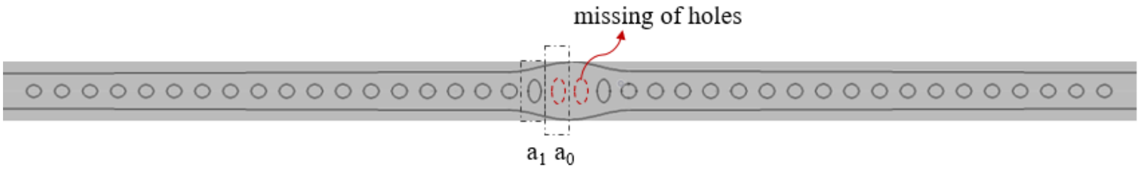

FIGURE 3.5: A sketch shows the parameters employed for optimization. Note that in this step of lattice constant optimization, no boundary holes are introduced yet.

The sweep of parameters as a function of quality factor and cavity resonance are displayed in Figure 3.6. The illustrations from left to right are the sweep as a function of quality factor and cavity resonance, as functions of a_0 and a_1; the top side presents the results for 450 nm wide cavity while the bottom side shows the 600nm wide cavity. The range of parameters in the sweep is shown in x- and y-axis. Color-bar shows the magnitude of the corresponding values. The quality factor is extracted by using Equation 3.2. Ten mirror holes are loaded on each side of cavity during the parameter sweep. The requirement of leaving more space around emitter in the 600nm wide cavity results in a much larger a_0 than in 450nm wide cavity.

From figure 3.6 (a) one can see that the maximum quality factor for the 450nm wide cavity is over 10^5. $a_0 = 170nm$ and $a_1 = 200nm$ are the optimized parameters. However, two aspects should be considered here. The first one is that the cavity resonance should be at the range of $930 \sim 940nm$, to couple with and enhance the QD emission. The second is a larger a_1 results in a less confined mode. A over large a_1 should be avoided because the coupling strength between emitter and cavity mode depends on the strength of the electric field at the position of the single emitter [12]. The cavity resonance wavelength increases with both a_0 and a_1. The lattice constants of 174nm for a_0 and 181nm for a_1 are chosen, which results in a cavity design with a quality factor of 4.5×10^4 and cavity resonance of 319 THz.

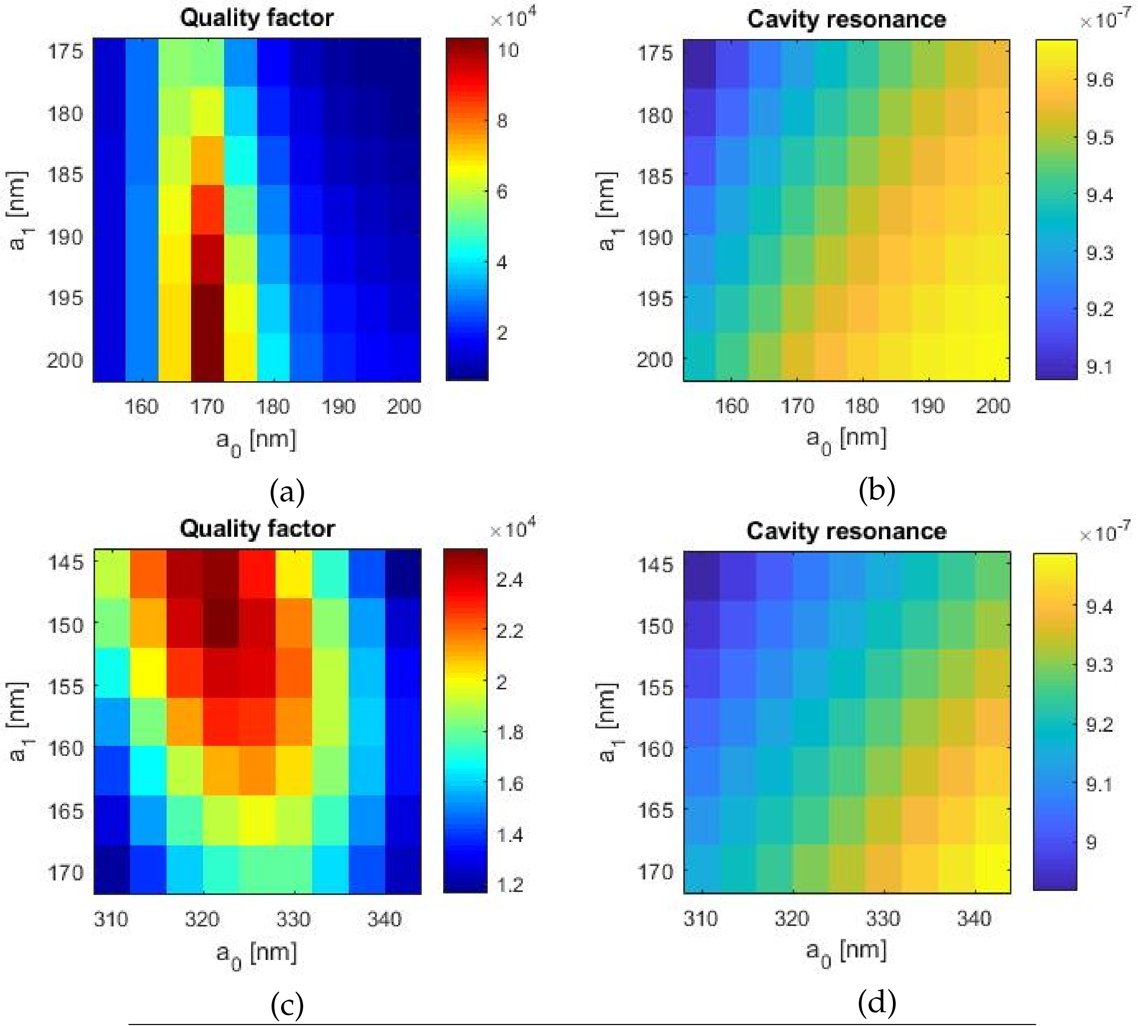

(a) (b)

(c) (d)

FIGURE 3.6: The sweep of lattice constants, as a function of quality factor and cavity resonance. (a) and (b) are the sweep for the 450nm wide cavity, while (c) and (d) show the sweep for 600nm wide cavity.

In comparison, the quality factor of 600nm wide cavity is much lower, due to the weaker confinement of cavity mode resulting from extended width and more missing holes. The highest achievable quality factor from Figure 3.6 (c) is over 2.4×10^4. The high-quality factors are more likely to occur with a small lattice constant a_1, but in this condition, the mode maximum is moving away from cavity center. Figure 3.6 (d) is the color map for the 600nm wide cavity. The cavity resonance is as a function of a_0 and a_1. It shows a similar trend with Figure 3.6 (b). Combined with the quality factor color map, the most suitable parameters can be chosen as $a_0 = 330$ nm, $a_1 = 162$ nm, resulting in a quality factor of 2.1×10^4, and 322 THz of cavity resonance.

3.4.3 The influence of boundary holes on the cavity

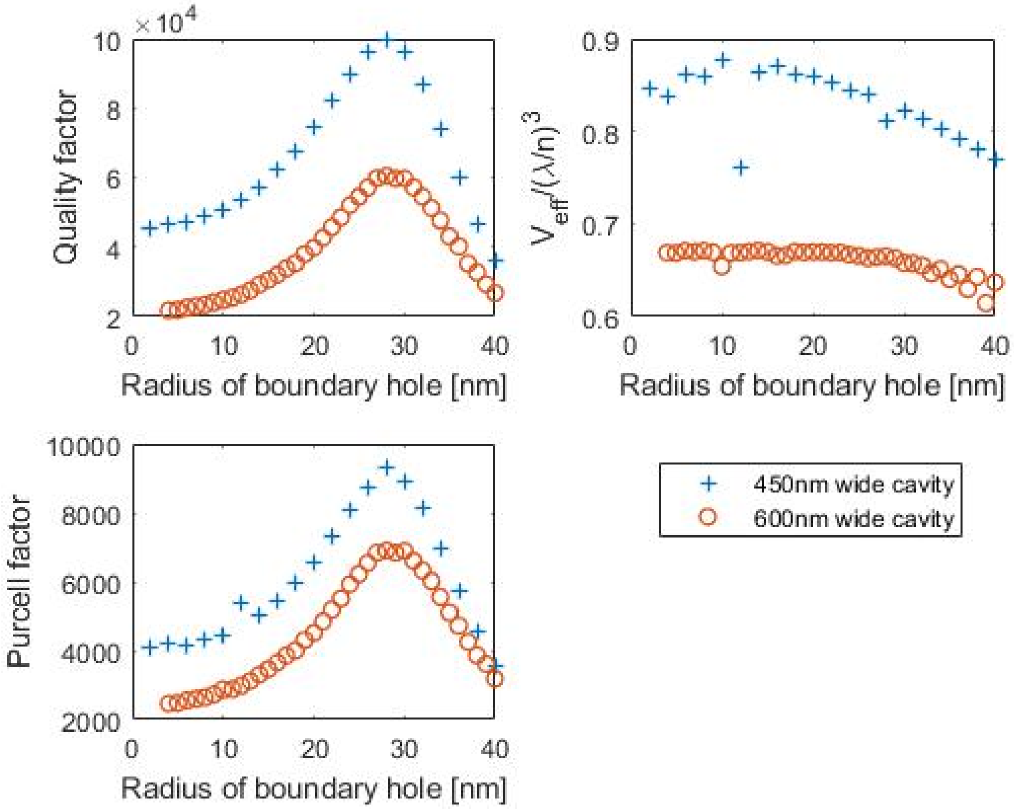

FIGURE 3.7: The performance wide cavity with different boundary hole size, in terms of quality factor, $V_{eff}/(\lambda/n)^3$, and Purcell factor. 10 mirrors are used to construct the cavity.

A half circular hole that is located in the edge of the cavity surface can enhance the quality factor of cavity further, without violating the rule of leaving enough space to the emitter. The added-on boundary hole is illustrated in Figure 3.4 (b) and (c). After the optimization of the lattice constants, the quality factor can achieve tens of thousands. Generally, the further improvement rely on the specific and accurate dimension and position of holes, for example, conduct a parametric sweep to a_3, however, this will not help a lot since the more outer side holes are less sensitive to the improvement of the quality factor. An alternative solution is to introduce a boundary hole in the cavity, which enables a better confinement of the optical modes.

The dependence of the cavity to the radius of the boundary hole is illustrated in Figure 3.7. The range is swept from 1 nm to 40 nm. An over large hole radius should be avoided due to the limitation of distance. Ten mirror holes on each side of the cavity are considered in the simulation. Overall, the quality factor is closely related with the radius of the boundary hole and the optimum occurs at around 28nm. Compared with the condition of no boundary holes are added, quality factors for 450 nm cavity and 600 nm cavity can be enhanced by a factor of 2.2 and 2.5, respectively. By contrast, the mode volume is not sensitive to the radius but still has a decreasing trend. Notably, the mode volume for 600 nm cavity is smaller, which is attributed to a better lattice constant induced sharper confinement to optical mode. The Purcell factor is calculated based on Equation 2.38, but a modification has been made to be more suitable for a dissipative medium [43]. The utilized equation is,

$$F = \frac{3}{4\pi^2}(\frac{\lambda_0}{n})^3 Re(\frac{Q}{V}) \tag{3.3}$$

where the mode volume V is expressed as,

$$V = \frac{\int [\tilde{\boldsymbol{E}} \cdot \frac{\partial(\omega\epsilon)}{\partial\omega} \tilde{\boldsymbol{E}} - \tilde{\boldsymbol{H}} \cdot \frac{\partial(\omega\mu)}{\partial\omega} \tilde{\boldsymbol{H}}] d^3\boldsymbol{r}}{2\epsilon_0 n^2 [\tilde{\boldsymbol{E}}(r_0) \cdot \boldsymbol{u}]^2} \tag{3.4}$$

The ratio of Q and V generates the Purcell factor, thus Purcell factor also exhibits a strong correlation with the radius of the boundary hole and experiences a similar enhancement. The Purcell factor is calculated based on an emitter positioned in the center of the cavity.

The variation of mode volume along increasing boundary hole radius can also be viewed from electric field distribution. Ideally, one would expect the electric field is accumulated around the position of the emitter, for effective coupling between cavity mode and the emission. Figure 3.8 displays the electric field distribution at a different radius, the x-axis represents the distance from the cavity center, while the y-axis shows the strength of the normalized electric field. Overall, the electric field is approximately even in the first few peaks and closely followed by a dramatic drop. For the more massive holes, the position with the strongest electric field is moving toward the center, appearing in a decreased mode volume.

Notably, the position of placing the boundary holes are crucial and sensitive to result. The optimum position should be at the where of second mode pattern located counting from the center; equivalently, it is the position of the second peak from left in Figure 3.8. Moreover, the length of sinusoidal outline tapering is a parameter that influences the quality factor, the overlong and over short span both yield a weak result.

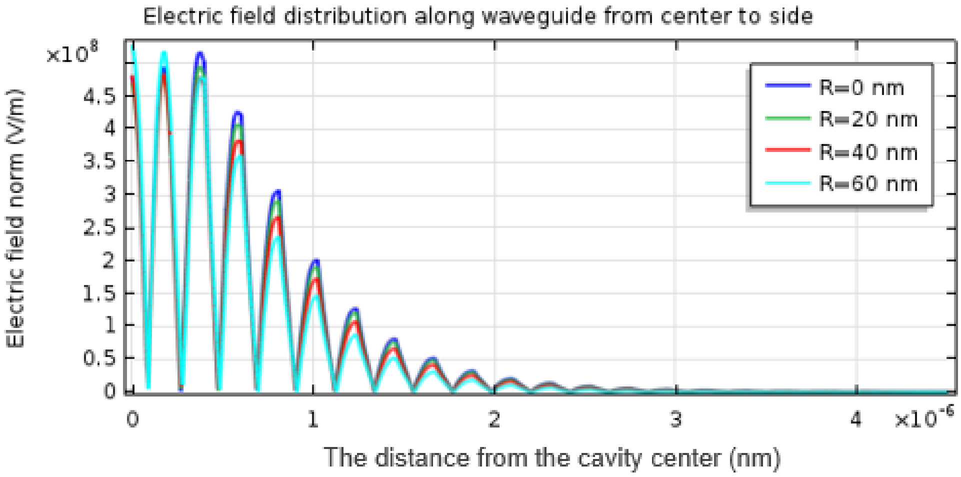

FIGURE 3.8: The electric field distribution from cavity center to waveguide, with variable of different size of boundary hole, evidencing mode profile improvement by larger hole size.

3.4.4 The influence of mirror elements on the cavity

After equipped with the optimum boundary holes, a certain number of mirrors are loaded to the cavity, to calculate the intrinsic quality factor and the corresponding scattering loss. The band diagram of the mirrors employed in this context is presented in Figure 3.2. By loading more and more mirrors in, the cavity becomes more and more decoupled to the waveguide. Meanwhile, the quality factor, indicating the rate of the energy loss of the whole system, is expected to be saturated to a specific value which is referred to the intrinsic quality factor, where the photon-loss is dominated by the scattering, instead of transmission.

Figure 3.9 shows the calculation to the quality factor, mode volume and the Purcell factor, as a function of the number of loaded mirrors on each side of the cavity. Similar to the investigation presented in Figure 3.6, The intrinsic quality factor for 450 nm cavity is approximately twice of 600 nm cavity, indicating the lower scattering loss with less missing holes in the cavity. The intrinsic quality factor can achieve 10^5 for 450 nm cavity and 6×10^4 for 600 nm cavity. The Purcell factor is calculated based on Equation 3.3 with a positioned emitter and follows a similar trend with quality factors.

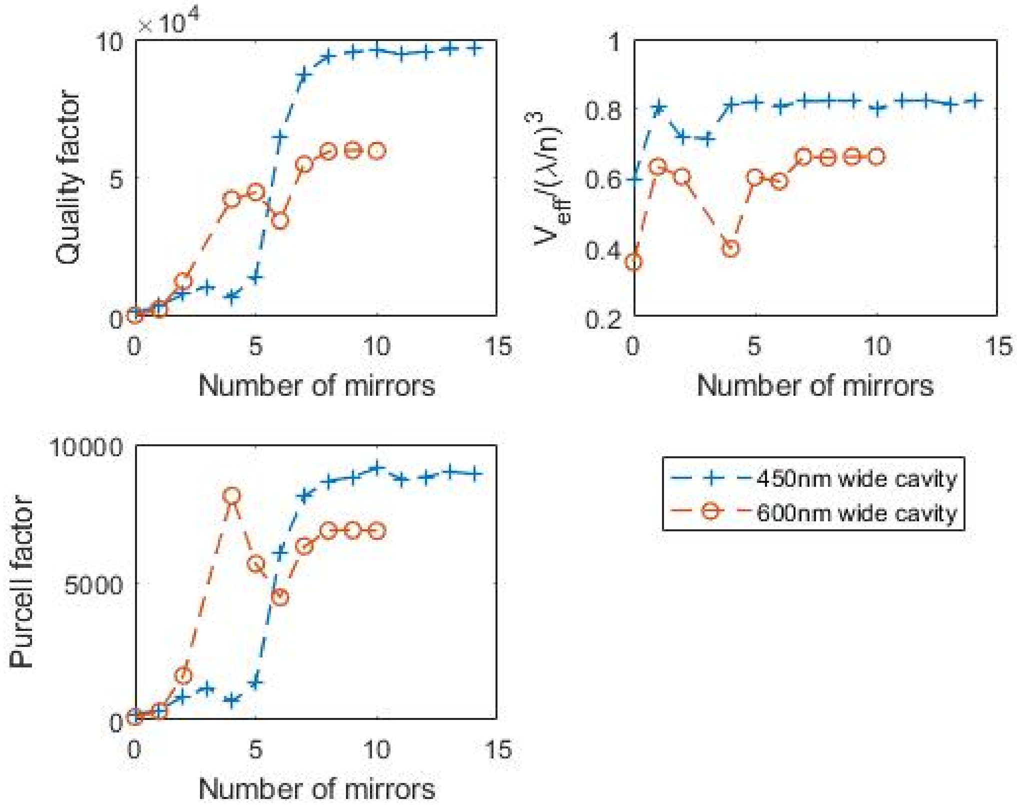

FIGURE 3.9: The performance of wide cavity with different number of mirrors coupled in, in terms of quality factor, $V_{eff}/(\lambda/n)^3$, and Purcell factor. The radius of boundary hole is 28 nm.

3.4.5 The transmittance of the cavity

A transmittance of near-unity through the cavity is always desired, from the perspective of effective extraction of photons emitted by the quantum dot. Transmission spectrum at cavity resonance is conducted and shown in Figure 3.10, via pumping light into the port of one side and collecting on the other side. For a photonic cavity without the tapered outline, the transmission at resonance can be calculated by [19, 38]

$$T = \frac{Q_{sc}^2}{(Q_{wg} + Q_{sc})^2} \tag{3.5}$$

where Q_{sc} is the intrinsic quality factor, which is determinate for a specific design and only dominated by scattering loss, as mentioned above. The Q_{wg} is the total quality factor for the cavity-waveguide coupled system. This equation conveys an important idea, which is, the value of Q_{sc} determines the upper limit of Q_{wg}, under the premise of relatively high transmittance. Therefore, in the realization such as the enhancement of decay rate that a high-Q cavity is wanted, Q_{sc} should be extremely high to ensure a considerable T, and this is another solid reason for the optimization to the cavity towards high Q_{sc} in the previous section. In practical aspects, the Q_{wg} with a high T is achieved by decreasing the number of loaded mirrors to the cavity.

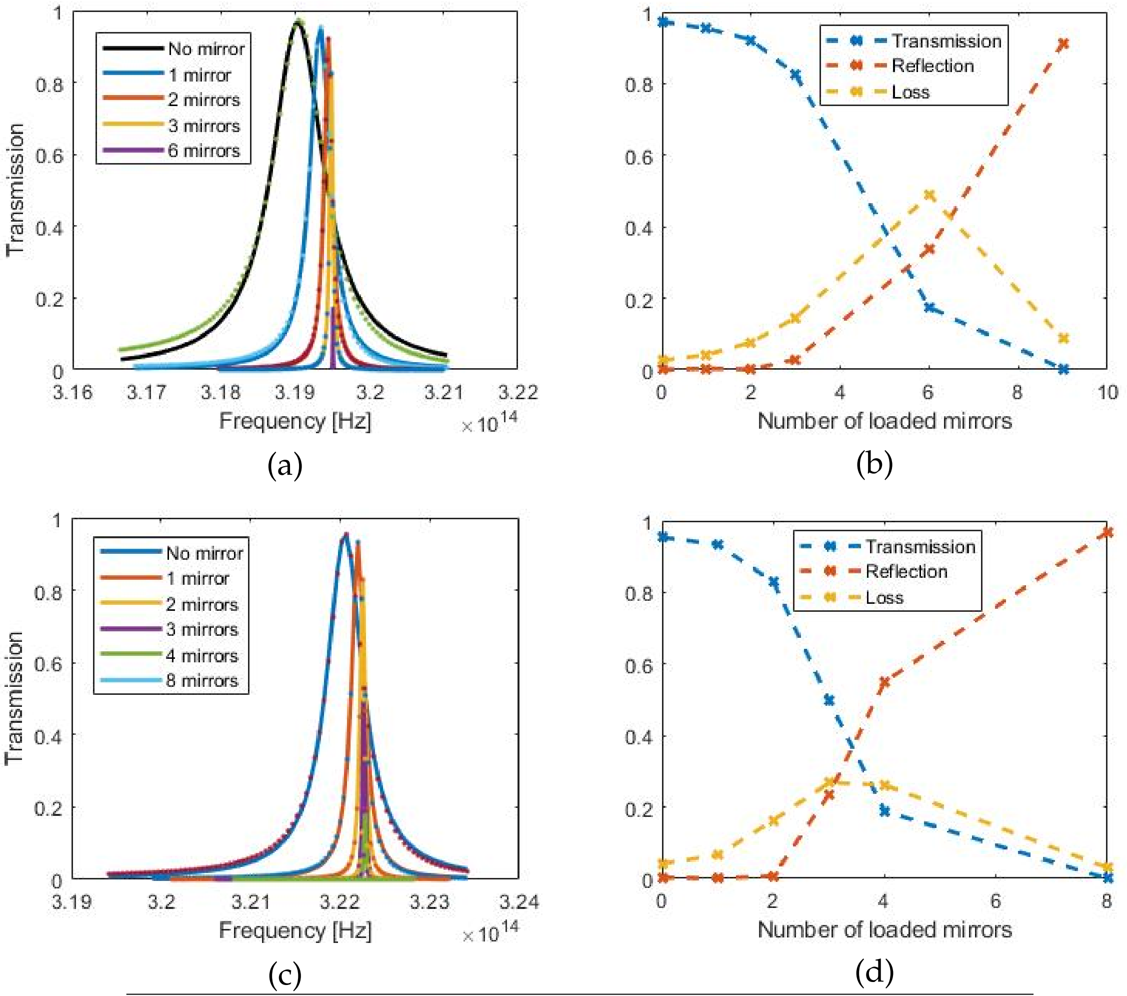

(a) (b)

(c) (d)

FIGURE 3.10: The transmittance at cavity resonance for (a) 450nm wide cavity and (c) 600nm wide cavity, and the plot of transmission, reflection and loss as a function of the number of loaded mirrors, (b) for 450nm wide cavity and (d) 600nm wide cavity.

Back to the transmission spectrum illustrated in Figure 3.10, the two figures on the top present the calculations for the 450nm cavity, which involves the transmission at cavity resonance, and the plot of transmission, reflection, and loss as a function of the number of loaded mirrors. The two figures on the bottom show similar calculations but for the 600nm cavity. Overall, loading more and more mirrors drops the transmittance as expected, but steeper for the cavity with a modulated outline. For a nanobeam cavity with a straight shape, the transmittance is 25% at least even if Q_{wg} equals Q_{sc}, according to Equation 3.5. However, the transmittance is only 1.7×10^{-3} for the 450nm cavity when coupled with nine mirrors, and 2.8×10^{-4} for the 600nm cavity after combined eight mirrors, although the performance for transmission with very few mirrors looks good. This difference indicates the mechanism of scattering loss for the cavity with the modulated outline is more than without modulation; in particular, the out-of-plane loss caused by the refraction at the air-semiconductor interface. Consequently, the number of coupled mirrors should not be a lot when transform to the fabrication process and the following measurement, to guarantee a relatively high extraction efficiency. Another aspect that should be noted is the blue-shift of cavity resonance with a different number of loaded mirrors, which is because a more confined cavity with increased mirror number, resulting to a shorter cavity length and therefore shorter resonance wavelength. The amount of shifting is significant for the first few mirrors and keeps nearly unchanged with many mirrors.

In the simulation, two ports are added to both sides of structure model, as illustrated in Figure 3.4 (b) and (c), one of them is set as the excitation source, and simultaneously collecting light from the both. Thus, the efficiency of transmission and reflection of the pump light can be calculated and also the loss can be extracted. Along with more and more mirrors coupled in, the transmission closes to zero, and the reflection closes to unity. The loss increases at the beginning and drops at the end, due to the coupling-in efficiency is rather low, and almost none of pumping light is transmitted after many mirrors loaded.

3.4.6 Temperature-dependent cavity resonance

Figure 3.11 shows that the cavity resonance reacts to the temperature from 6K to room temperature. The QD-cavity coupled system should be operated at a cryogenic temperature to investigate the interaction, due to de-phasing of QD originated from the phonon influence. Furthermore, the process of *detuning* is to adjust the degree of spectral matching by varying temperature. So how the cavity resonance based on GaAs material reacts to the temperature is worth to study. The index of effective refractive is referred to as [44]. In conclusion, the cavity resonance varies linearly with temperature and the resonance shift is approximately 16 nm from 6K to room temperature.

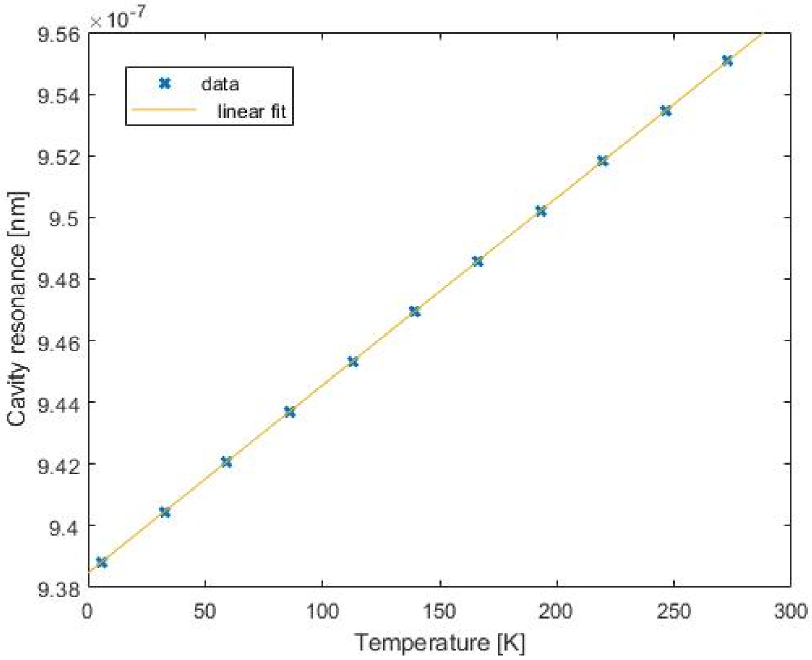

FIGURE 3.11: The simulation of dependence between cavity resonance and temperature, based on the GaAs effective refraction index from [44].

3.5 Cavity simulation with embedded dipole

In the previous section, we assume the QD is positioned in the center of the cavity, to calculate the Purcell factor. However, in this thesis work, the self-assembled QDs of the samples are randomly grown on the wafer with randomly oscillating direction. Therefore, it is necessary to figure out how theses two random factors influence the Purcell effect applied to the embedded emitter.

For a dipole with arbitrary oscillating direction, we can project the oscillation into x- and y- axis. The calculated Purcell factors along these two orthogonal directions are then noted as Px and Py, which have inserted x- and y- projection of the $\tilde{E}(r_0)$ into Equation 3.4, respectively. Figure 3.12 (a) and (b) map out the calculated Px and Py at every positions in the cavity. The discontinuity of Purcell factors is presented in the boundary of GaAs and air as expected, due to the significant difference in refractive index. Assuming that only the area in the cavity center is interested, there is an apparent contrast between Px and Py emerged from comparing the Figure 3.12 (a) and (b), proving the effectiveness of the designed cavity. Overall, Figure 3.12 (a) and (b) have revealed how an arbitrary embedded QD response to the cavity, in terms of the Purcell effect. Figure 3.12 (c) illustrates the logarithm of the proportion of Py and Px. By measuring the fast and slow decay rate of the QD, and calculating the proportion of them, the more accurate possible positions where the QD locates can be speculated. The curve of magenta color is an example for this and will be introduced in Chapter 6.

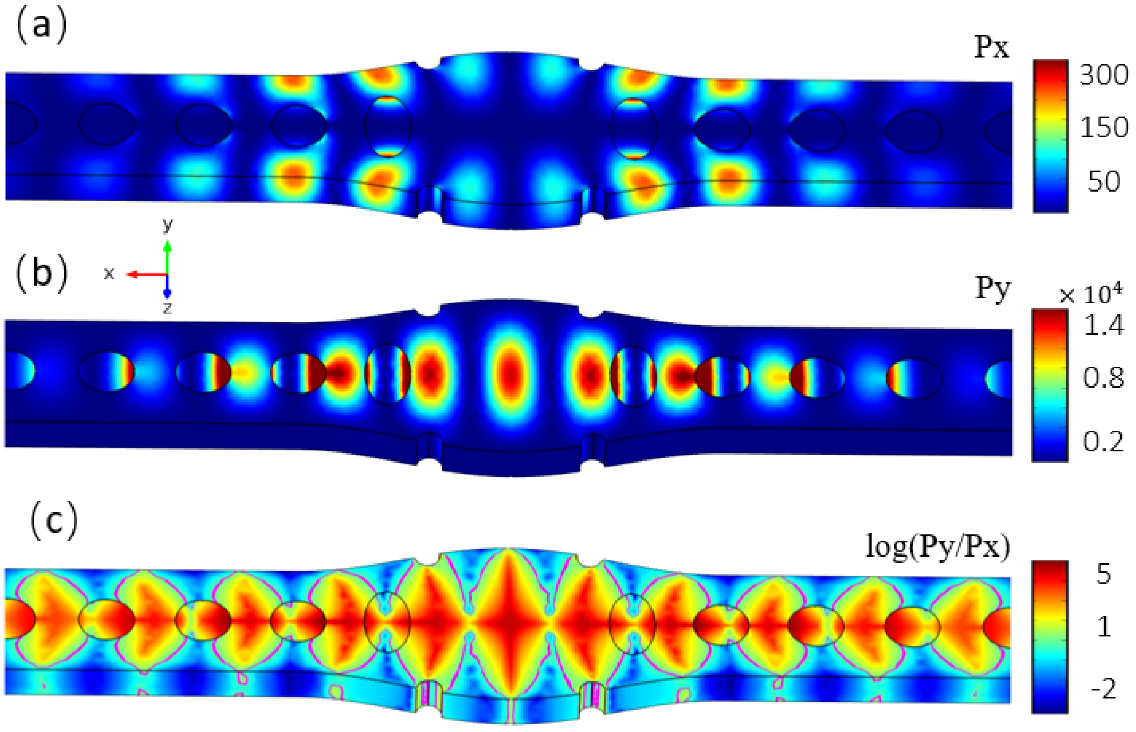

FIGURE 3.12: The calculated Purcell factors at every positions in the cavity, for a dipole oscillating along (a) x- and (b) y- direction. (c) shows the logarithm of proportion of Py and Px.

Chapter 4

Introduction to Sample

This chapter introduces the fabrication of the sample, primarily, three key processes, electron-beam lithography, dry etching, and wet etching are elaborated in section 4.1. Some SEM images showing the patterned nanobeams with different scopes are shown in section 4.2.

4.1 Fabrication process

The investigated InAs quantum dots are embedded into a thin layer (160 nm) of GaAs on top of AlGaAs which serves as sacrificial layer. The raw sample is grown in the group of Prof. Wieck. The nanofabrication is carried out by members (Zhe and Asli) of the Quantum Photonics Group under the supervision of Leonardo Midolo. The layer structure of the nanobeam sample before nanofabrication is shown in Figure 4.1 (a). Size of the chip is 5mm × 5mm. The fabrication of the sample includes three steps in general, which are electron beam lithography, dry etching, and wet etching processes. The nanobeam sample is patterned by using the recipe of ZEP520 (Elionix 125keV) that is designed for all GaAs substrates. An example of patterned sample is shown in Figure 4.2. The processing time takes approximately one day but was not executed with this thesis work. The recipe consists of 6 steps as following:

(1) Clean wafer: Flush the sample with acetone and IPA, then immediately blow dry by nitrogen.

(2) De-oxidation: Put the sample in diluted phosphoric acid (1:10) for 1 minute

(3) Adhesion layer: Evaporate 2 nm of Ti for improved ZEP adhesion.

(4) Spin-coat: Spin-coat Zep 520 resist at 2050 rpm for 60s, and then bake on hot plate at 185C for 5min.

(5) E-beam exposure: Expose patterns with PEC by Elionix F125 (125kV) with a clearing dose of 350 uC/cm^2.

(6) Development: Develop 60s in n-Amyl acetate that has been cooled down to -5C, then rinse in IPA for 10s, and followed by nitrogen dry.

4.1.1 Electron-beam lithography

Electron-beam lithography is a crucial step carving out the custom shape on the thin layer of GaAs, by shining a focused beam of electrons to the surface coating. As shown in Figure 4.1 (b), a very thin film (ZEP) is covered on the surface, which is a high-performance positive electron-beam resist. The scanning electron beam changes the solubility of resist, causing the shined area being removable with dry etch. Notably, the figures only depict the principle and steps of fabrication, without showing the exact surface pattern of structure.

4.1.2 Dry etching

After electron-beam lithography, the pattern can be removed by exposing a plasma of reactive gases (Cl_2 and BCl_3). The process can empty the materials which has no ZEP covered above, as Figure 4.1 (c) depicted. In contrast to the wet etching, the dry etching has the unique ability to conduct an anisotropic etching, which is preferred for fabricating a nanostructure with deep holes. Then the ZEP resist is removed by NMP at 70C for 10min, cleaned by IPA and dried by nitrogen.

4.1.3 Wet etching

Wet etching is a supplemental process to dry etching which uses liquid chemistry to remove the underlying of thin GaAs membrane. Etching time determines the length of the etches along the substrate surface. Figure 4.1 (d) shows the process by the HF solution, and it can be seen that the border of the etched area can exceed the border of dry etching and make it hollow. As a result, the GaAs nanostructure will be overhead and surrounded by air. Figure 4.1 (f) is the SEM image with aerial view, showing the hollow underlying and overhead structure.

Several different liquid chemicals are used for the wet etching of the wide cavity. In the beginning, the sample is placed inside a boat and immerses in HF solution with 5% concentration, soaking time is kept to 30s. Afterward, the liquid changes to H_2O_2 to remove photoresist residual. Then H_3PO_4 (1:10) is used to clear oxide layer. At last, the liquid is replaced by IPA to prepare for critical point dryer. Every time for liquid exchange, a certain amount of water is necessary to dilute residual liquid.

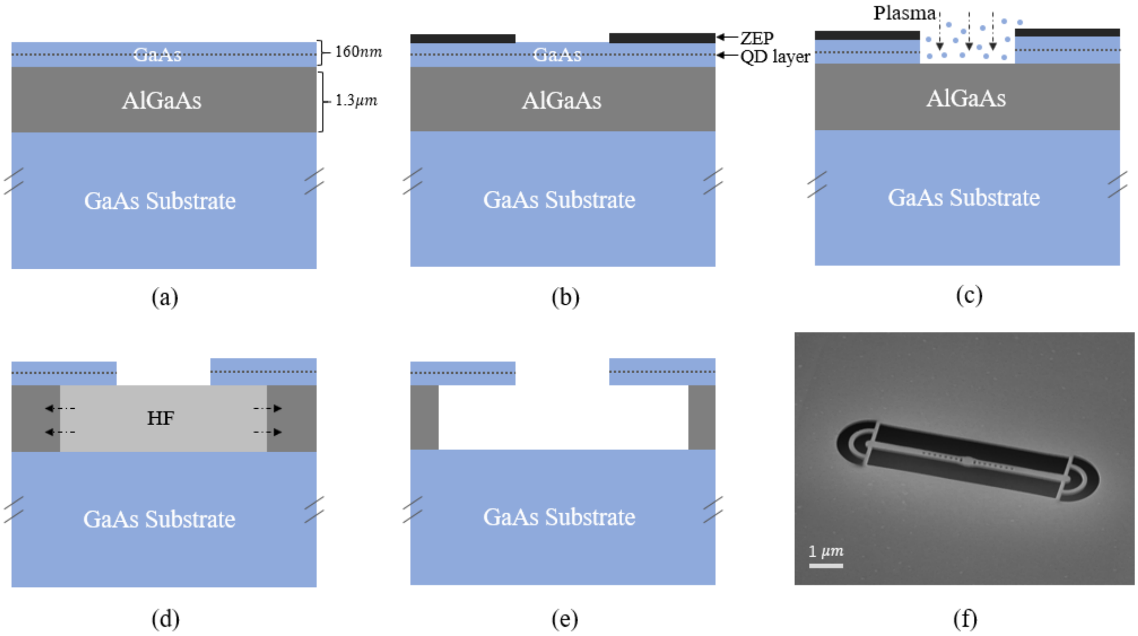

FIGURE 4.1: Schematic diagram of the fabrication process. (a) shows the layer structure of sample before nanofabrication. The electron-beam lithography process is depicted by (b) in which ZEP is covered on the sample surface. (c) and (d) are the processes of dry etching and wet etching, respectively. (e) shows the overhead GaAs membrane after nanofabrication and (f) is an aerial view to the realistic after-fab structure.

4.2 Scanning electron micrograph of structures

Figure 4.2 shows three SEM images with different scopes. It is notable that the fabricated structures are only wide cavity with 450nm width, with sweep parameters of outside hole radius and the number of loaded mirrors. The radius of the outside hole is varied from 20nm to 40nm with a 10nm interval, for each different radius, the number of coupled mirrors can be 1, 2, 3, or 9.

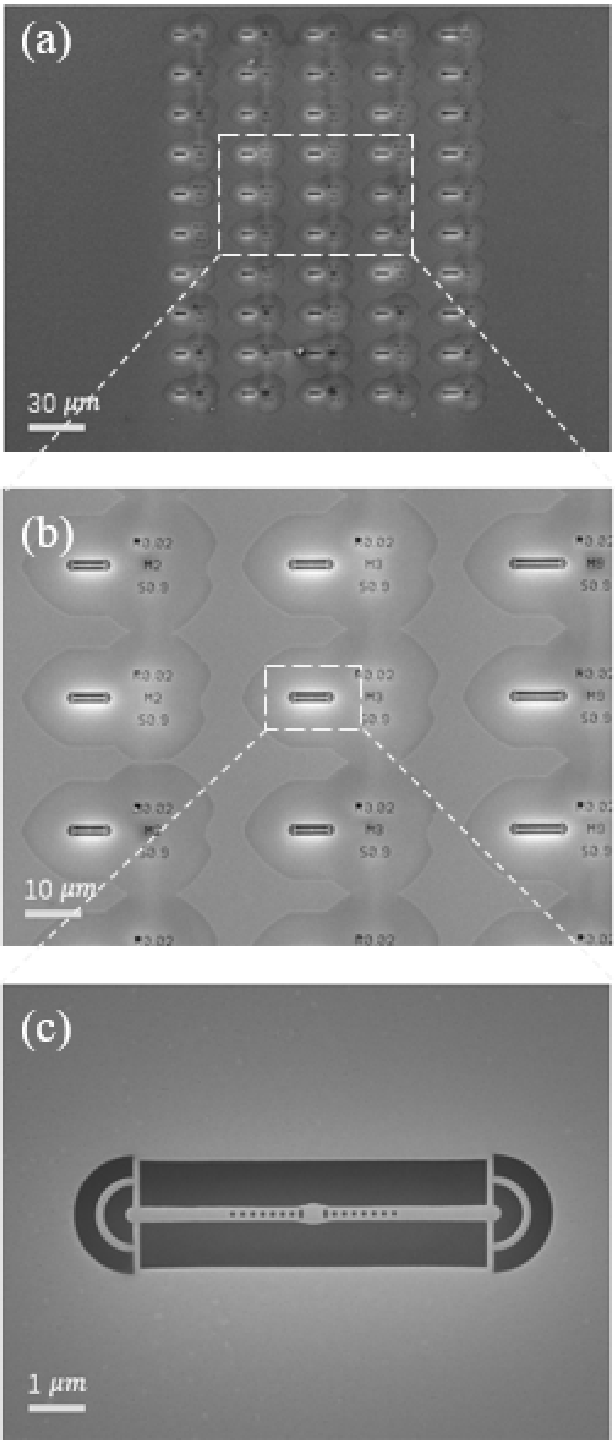

FIGURE 4.2: SEM pictures to the sample with different scopes.

Chapter 5

Experimental investigation at Room Temperature

This chapter introduces the experimental work at room temperature, which aims at characterizing the resonance wavelength and quality factor of the wide cavity. The first section (Sec. 5.1) of this chapter introduces the optical setup, which is then followed by the measurement results in the section 5.2. In addition, we introduce the coupling of light into the cavity and demonstrate a preliminary transmission spectrum. Lastly, a statistical analysis is given for the cavity structures with different geometrical parameters.

5.1 Optical setup

Figure 5.1 shows a schematic representation of the experimental setup at room temperature for the transmission measurement of the (wide) cavity structures. A super-continuum laser light (SuperK, NKTphotonics) is used as a broadband light source, which is utilized in combination with a spectrometer to investigate the resonant transmission peaks within a wide wavelength range (780 nm - 1130 nm). The laser light is coupled into the (wide) cavity through a on-chip circular grating coupler after passing through multiple beam splitters (BS). The leftmost BS is used to couple a white-light source (WS) into the optical setup, which is the light source for the imaging. The middle BS is used to guide the signal into the spectrometer, via the reflections from two mirrors which provide the freedom that is required to adjust the beam direction. Then, the propagated light passes through the rightmost (50:50) BS and its reflection port is aligned with the detector head of the power meter (Thorlab PM100D)) for monitoring the input power, as a reference. The second port of the middle BS is aligned to the charge coupled device (CCD) camera for displaying the images of the structures, which are reflected back on the CCD through the BS. The spectrometer is equipped with low (800 g/mm) and high (1200 g/mm) resolution gratings to diffract the incoming light. An optical density filter of 2.0 is used here for ensuring the detection intensity of the spectrometer to be far away from saturation. The sample is mounted on a three-axis translation stage and positioned in the focal area of the objective lens.

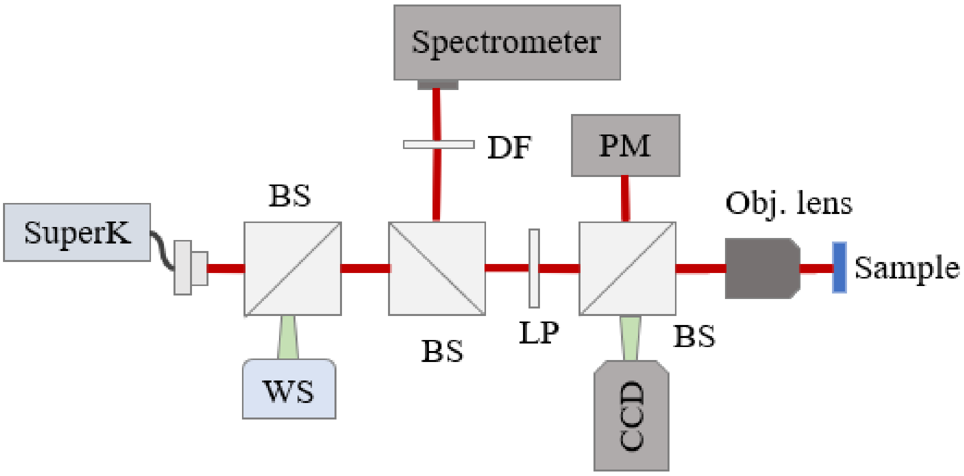

FIGURE 5.1: Schematic of the experimental set-up. Simplified experimental setup for the optical characterization. The optical signal is derived from a SuperK laser is sent into a (50:50) BS, where half of the light is coupled in to the WS in order to be used for imaging. The light propagated through the leftmost BS is then splitted into two by the second BS(50:50). Lastly, the propagated light is coupled in to the structures on the sample through the objective lens to perform the transmission characterization at room temperature and pressure.

5.2 Transmission measurements

5.2.1 The alignment of in- and out- coupling light

This section explains the optical characterization of the wide cavity, in particular, the influence of the number of mirror holes and the size of the boundary hole on the cavity quality factor and resonance wavelength. Sixty geometrical structures with different parameters are measured and characterized. Specifically we designed (and fabricated) three different groups of structures, which are coupled with 1, 2, or 3 mirror holes on each side of the cavity. For each from the groups, the boundary hole size is tuned from 20 nm to 40 nm, as illustrated in the inset of the Figure 5.4. The transmission measurement is by the SuperK laser source on one of the circular grating couplers (that are patterned to be on the sides of the cavity, as seen in the Fig. 4.2 (c)) which is then assigned as the input coupler. The transmitted light through the cavity is collected through the second circular grating coupler (output coupler). A grating coupler is a periodic structure with several grating teeths that are able to couple the light directed on it vertically (out-of plane) to the waveguide mode. The type of the vertical coupler used here can provide a coupling efficiency as much as 10%.

The in-coupling of light needs to be optimized for the effective light extraction. One of the important criterion is to provide a sufficient overlap between the collection port and the transmitted light. This alignment process is done by vertically shining the defocused laser pattern into the input coupler, in order to display a bright transmitted light for bringing the collection port to the bright spot.

In Figure 5.2, we demonstrate a successful coupling between light and the cavity. The difference between the brightness on the input and output couplers indicates the low efficient coupling of the grating couplers. In addition, the light pattern, seen in the middle of the cavity points out that there are considerable amount of leaky modes due to the scattering.

5.2.2 Transmission spectrum

The transmission response of the cavity is monitored based on the direct detection method shown in the Figure 5.3. The multi-terms Lorentz fit is applied to the initial data points to treat different contribution individually; meanwhile, it helps to analyze the origins of the peaks. The R-square of the all-inclusive fit is 0.9194. Overall, two peaks have manifested stronger brightness and narrower widths than the others, which corresponds to different mode-field distributions as shown in Figure 5.3 (b) inset. This transmission spectrum is supported by the FEM simulation presented in Figure 5.3 (a). The deviation of the specific wavelength and the interval over peaks between the FEM simulation and the experimental result is attributed to the fabrication deviation. The peaks other than two sharps are possibly resonant modes spaced by free spectral range (FSR), generated from the boundaries of two circular grating couplers.

The sharp peak at 941 nm has a narrow linewidth of 0.98 nm extracted from the Lorentz fit, resulting in a quality factor of 960, based on the equation,

$$Q = \frac{f_0}{\Delta f} \approx \frac{\lambda_0}{\Delta\lambda} \tag{5.1}$$

where $\Delta\lambda \approx \frac{\lambda^2}{c}\Delta f$ is used to convert the spectral width into wavelength unit [45]. This peak corresponds to the fundamental cavity mode in which the mode-field is confined in the center. Similarly, the other sharp peak which is classified to a second order mode has a central wavelength of 960 nm and FWHM of 3.79 nm, corresponding to a Q-factor of 253.

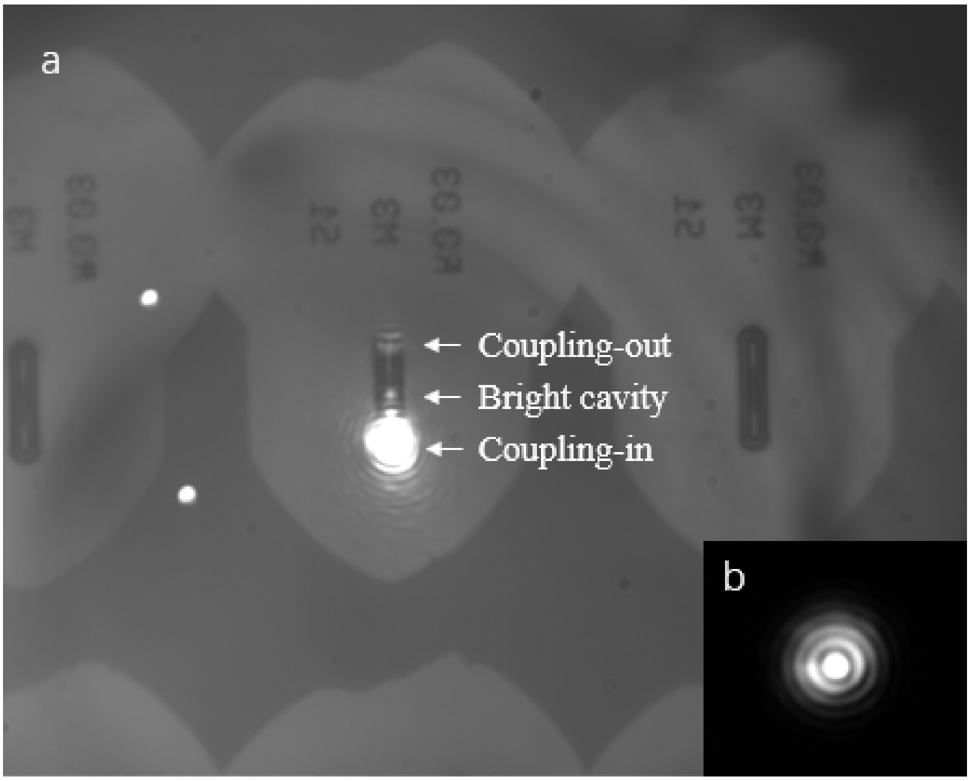

FIGURE 5.2: Alignment of the pump laser light on the circular grating coupler. (a) The CCD camera image shows in- and out- coupling between laser light and the circular grating couplers. The bright spot above the cavity is emerging from the leaky modes. (b) a defocused beam pattern on the bulk area.

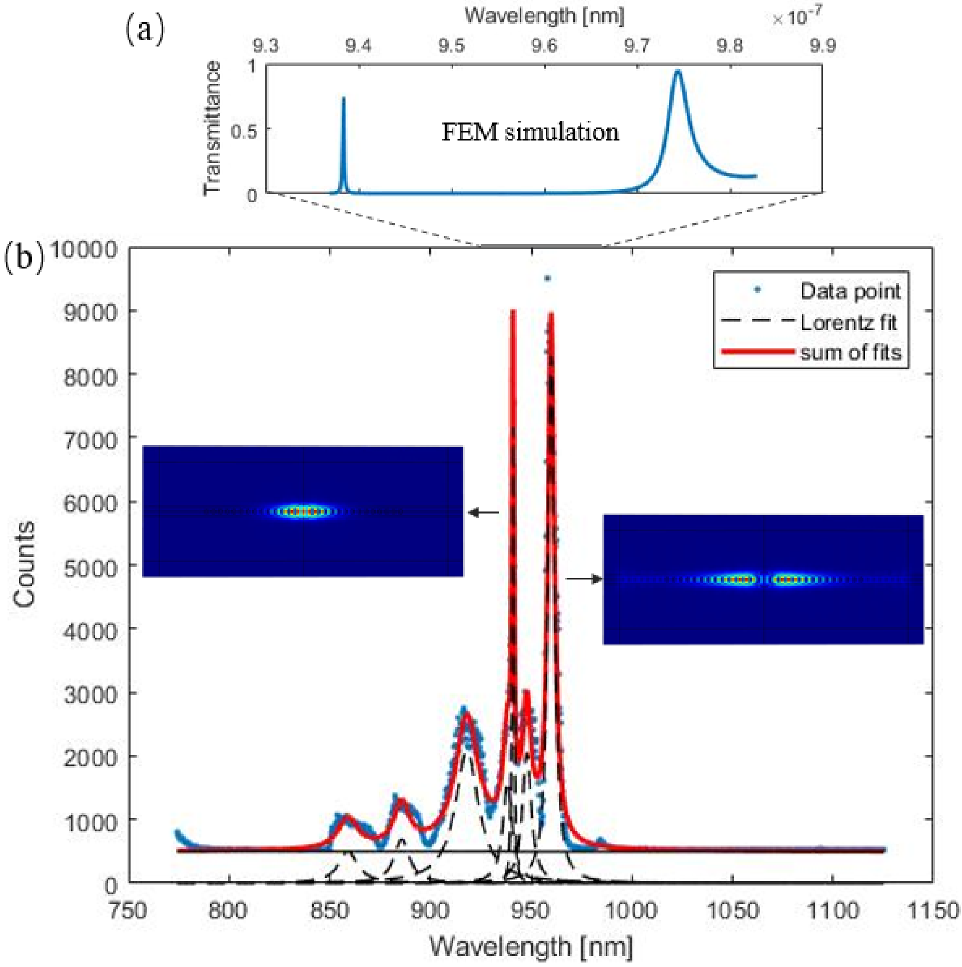

FIGURE 5.3: An example of the transmission spectrum for the cavity coupled with three mirror holes on each side. (a) A verified transmission spectrum by FEM simulation. (b) the experimental transmission spectrum. Two sharp peaks corresponding to different mode profiles that is depicted by inset illustrations. The black dashed line represents the Lorentz fit applied to recorded data points(blue dots), while the solid red line shows the sum of fits over the Lorentz fits and baseline.

5.2.3 Statistics of cavity quality factor of 60 copies

Figure 5.4 shows a plot of the transmission measurement results over 60 structures at room temperature. These 60 structures are classified by both the number of mirrors and the radius of the boundary holes, as mentioned above. The number of mirrors that have been loaded to each side of the cavity is represented by *n* in the figure legend, correspondingly, the red dotted box in the inset figure illustrates the number of mirror holes from one to three. The triangular, circle and square represents the boundary hole size of 20 nm, 30 nm, and 40 nm, respectively. The profile of the boundary holes is depicted in the inset figures by blue dotted circles. For the sample, the actual boundary hole size is hard to be extracted from the scanning electron micrograph (SEM) pictures due to the non-round hole shape. Because of that case just the design hole sizes are analyzed.

Conclusively, the quality factors show an absolute dependence on the number of mirrors, whereas the reliance on the boundary hole size is not as significant. From the statistic plot, we can deduce that the quality factors from just one mirror loaded on each side of the cavity are principally distributed between 400 - 500. For the two mirrors, the Q-factors have an broad distribution around 600. The scattering distribution is more extensive for three mirrors, the low Q-factors below 300 and high Q-factor above 1100 can be found. One reason for the ambiguous dependence on the boundary hole size is the fabrication deviation, that caused the incomparability between structures with different hole sizes; the second reason could be the fabricated non-round outline shape caused by the E-beam etching process has raised the scattering loss. It is worth noting, that the possible short coherence time of the broadband superK limits the quality factor that could be determined.

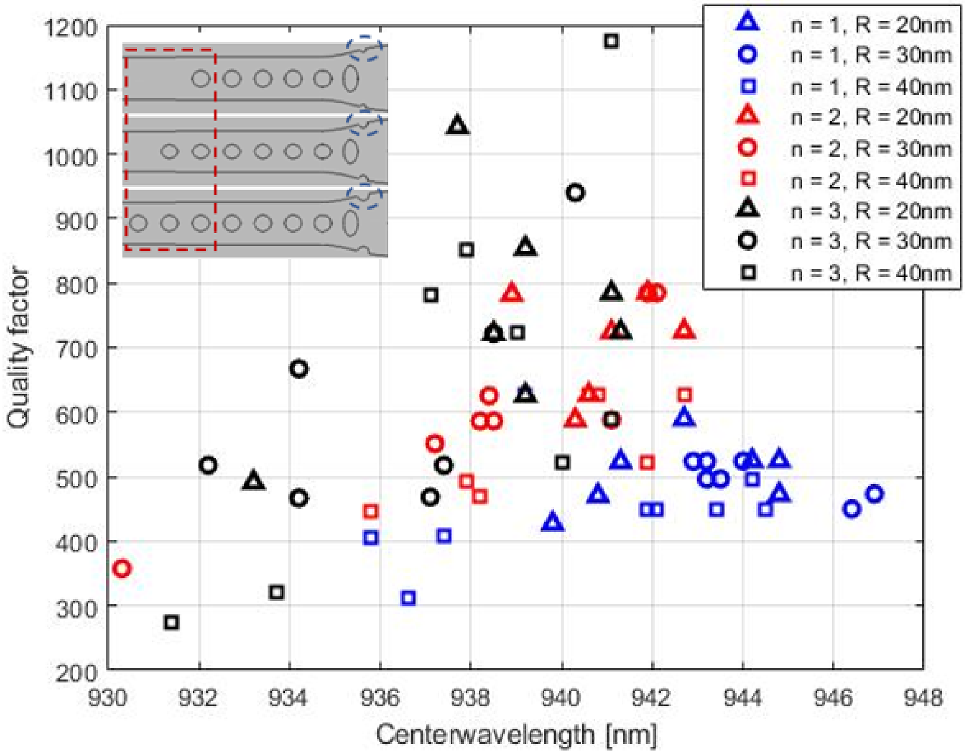

FIGURE 5.4: The quality factors from the 60 copies are statistics of the function of cavity resonance. The different symbols and colors represent the following: triangular - 20nm boundary hole radius; circular - 30nm boundary hole radius; square - 40nm boundary hole radius; blue - 1 mirror hole coupled on each side; red - 2 mirror holes loaded on each side; black - 3 mirror holes coupled on each side. The inset figure points out how the different parameters look like in the structure: the red dotted box shows the combined number of mirror holes from 1 to 3; the blue dotted circle exhibits the profile of the boundary hole with different sizes.

Chapter 6

Experimental investigation at Cryogenic Temperature

This chapter presents the experimental results at cryogenic temperature, to primarily study the modification of spontaneous emission of QD in a cavity. Section 6.1 introduces the optic setups of the experiment, where we perform photoluminescence (PL) measurements and lifetime measurements. The former aims to characterize the spectral separation between the cavity mode and QD emission, and the results are introduced in section 6.2. The lifetime measurement is used to determine the decay rate of spontaneous emission at different temperatures, detailed in section 6.3. In the last part, results from the two measurements are correlated and discussed.

6.1 Optical setup

The experimental setup is shown as a sketch in Figure. 6.1. The sample is mounted inside cryostat (Montana Instruments) which is equipped with a microscope objective (NA = 0.85, Olympus). The sample sits on a piezo motion controller (attocube systems, AG) that allows a three-axis displacement. The Montana cryostat uses the pulse-tube refrigeration technique with precise temperature control so that a range from 6K to room temperature is achievable in mK resolution. A turbo pumping station (Pfeiffer Vacuum, HiCube 80 Eco) is used to maintain a high vacuum environment. The vacuum is important in order to avoid H_2O crystal forming on the sample when we cool down. The pumping process normally takes several hours, and in the end, the pressure is down to around 1×10^{-6} mBar. The Ti: Sapphire laser (Spectra Physics, Tsunami) is used to excite the InAs QDs with 780 nm laser in the above band-gap excitation scheme, in which the incoming photons drive the electron to the conduction band of the GaAs material, then the electron spontaneously decays to the conduction band of the QD, and is closely followed by a combination with a hole in the valence band of the QD by emitting a photon. The spent time for this process is dependent on the lifetime of the QD emission at a specific temperature. Therefore, the measured lifetime should be in principle longer than the strict decay time determined from a resonant excitation scheme [46].

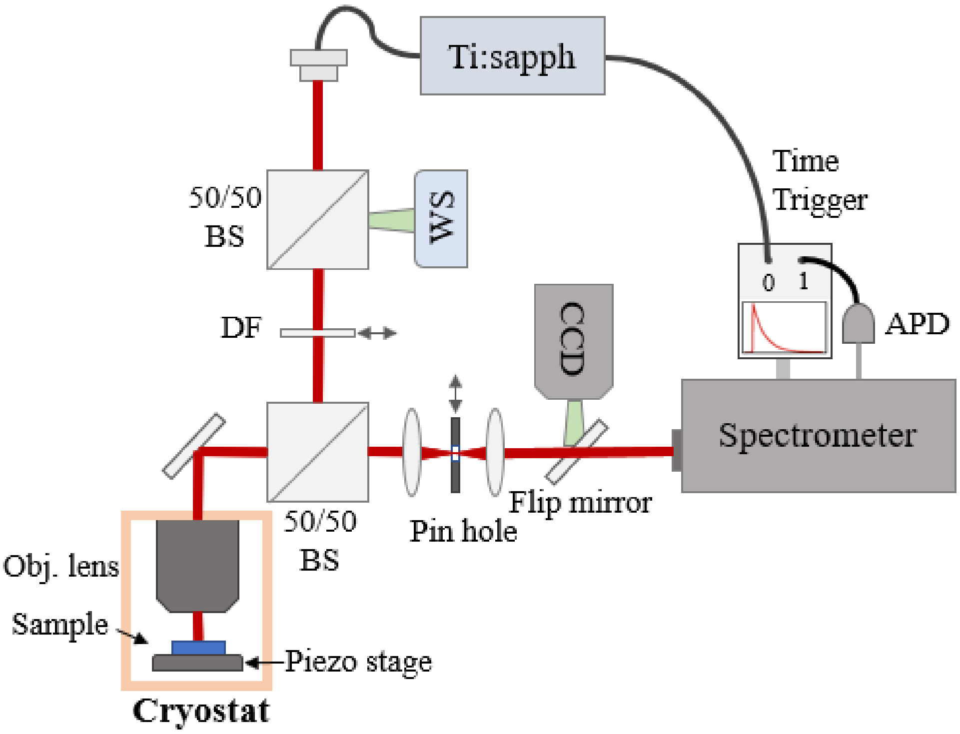

FIGURE 6.1: Schematic of the experimental set-up.

The sketch of setups can be seen in Figure 6.1. Two 50:50 beam splitters are used here. Following the light path deriving from the laser source, the first beam-splitter(BS) plays the role of coupling in the broadband white light source in, in order to image the sample. An optical density filter (DF) is used to control the excitation intensity. The pinhole is a useful tool to block the signal from unwanted background and only focus on the QD. On the collection side, the signals can either go into a CCD camera (Andor, iKon) or a spectrometer (Oxford Instrument, Andor SR500-B1) by a flip mirror. Furthermore, there is another flip mirror inside the spectrometer to either analyze the emission spectrum, or to take a decay curve to determine the lifetime.

6.2 Photoluminescence Spectroscopy

After the transmission measurement at room temperature investigating the cavity resonance characteristics, the sample is moved into the cryostat and cooled down to 4K. The QDs should be placed in a cryogenic environment to minimize the phonon dephasing induced by thermal interaction. The QD emits an insufficient amount of photons above ∼35K.

For maximizing the coupling strength between the quantum dot and the cavity mode, spatial, spectral, and polarization overlap needs to be achieved. In the case of spectral- and spatial-mismatch the coupling is reduced and leads to a reduced Purcell effect. This is particularly difficult to achieve as the self-assembled QDs of our samples are randomly grown on the wafer and the emission wavelength is also different for each QD. By fabricating many copies of the same structure, there is a higher probability of finding a perfect coupled system between single QD and cavity.

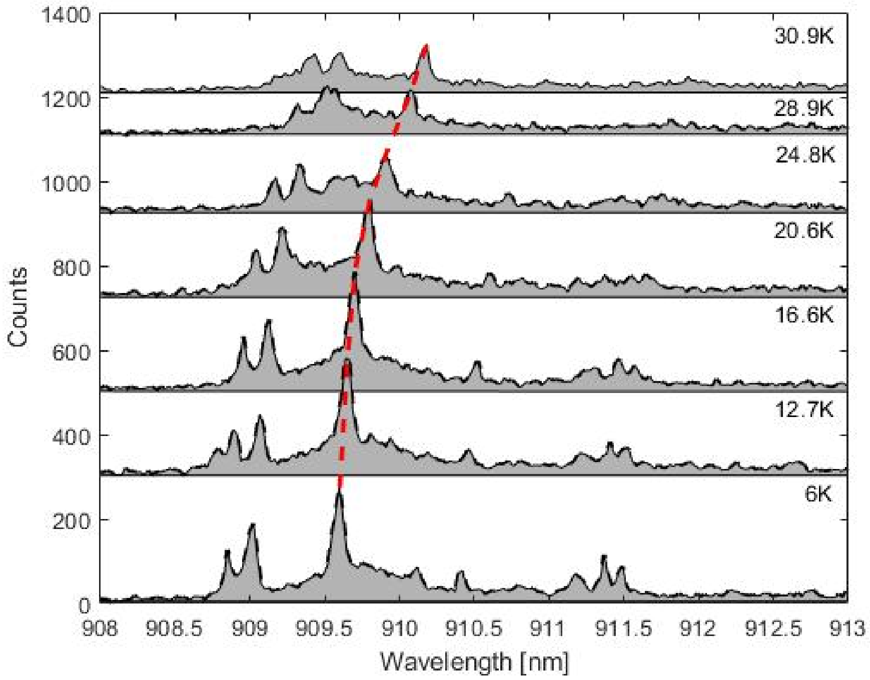

FIGURE 6.2: The photoluminescence at different temperatures, under an excitation power of $100\mu W$, displaying temperature-dependent tuning of QD emission wavelength. The red dotted line shows the wavelength shift of the QD emission that is being investigating.

The cooling down of sample should make the cavity resonance of the nanobeam structure undergo a blue shift, due to the temperature-dependent refractive index of GaAs. Although the change of refractive index with temperature of GaAs is well understood and the simulations can predict the wavelength tuning of the cavity resonances, a precise prediction is not possible due to unknown sample parameters, such as the dimension of non-round boundary hole. Therefore, the spectral position of cavity resonances is determined by the high-power photoluminescence measurement where the power-broadened lines of QDs allow us to see the cavity resonance. In the bulk area, i.e. unpatterned area, the quantum dot density is very high, and single spectral lines are hard to be resolved in the spectrometer with the 1800 L/mm grating. However, in the nanostructures, single quantum dot lines can be resolved. So the experiment and results shown in this section will only focus on the structure with QD coupled in.

Figure 6.2 shows the measured PLs at different temperatures, under an excitation power of 100 μW. The emission wavelength of QD experiences a red-shift with increasing temperature, whilst the intensity of the emission drops.

6.2.1 Multi-fit to photoluminescence

The high density of QDs on the wafer and the existence of a cavity suggests that the PL spectra should be fitted with a Gaussian and a Lorentz function at the same time. Figure 6.3 shows the fitting to the PL spectra collected under an excitation power of 40 μW, at 6K and 30.9K. As mentioned before, the actual temperature of the sample itself might be higher than of the environment due to the silver paint between the holder and the sample. The wavelength range of the PL spectra is from 890 nm to 930 nm and only the region between 909 nm and 912 nm displays peaks, thus we assume this is where the cavity resonance is located. The profile of multi-peaks in the PL spectra look like individual QDs with different spectral detuning from cavity resonance, which leads to the center peak being stronger than the side peaks. To prove whether the emissions are enhanced by the cavity, a fitting function with a combination of Gaussian and Lorentz profiles is applied to raw PL spectra. The mechanism of adding the individual fits to the peak strongly depends on the count rate and the profile of the target emission. Therefore, the number of fitted QDs in the PL at 30.0K are less than at 6K.

The R-square of the fitting is 0.91 for the PL at 6K and 0.83 at 30.9K. The blue curve represents the fitted QDs emission, while the red curves show the cavity profile. The pink curve illustrates the sum over the different contributions. One notable fact on this fitted PL spectra is that the QD exhibiting the strongest count rate has a shorter wavelength than the cavity resonance at 6K, in other words, a negative detuning. At 30.9K, the QD emission has already been tuned to a larger wavelength than the cavity resonance. This roller coaster detuning indicates the

QD and cavity resonance can be coupled spectrally at a temperature between 6K and 30.9K. Therefore, the QD with the most robust brightness has been investigated, and the corresponding information are extracted from the fitting and will be detailed in section 6.2.3.

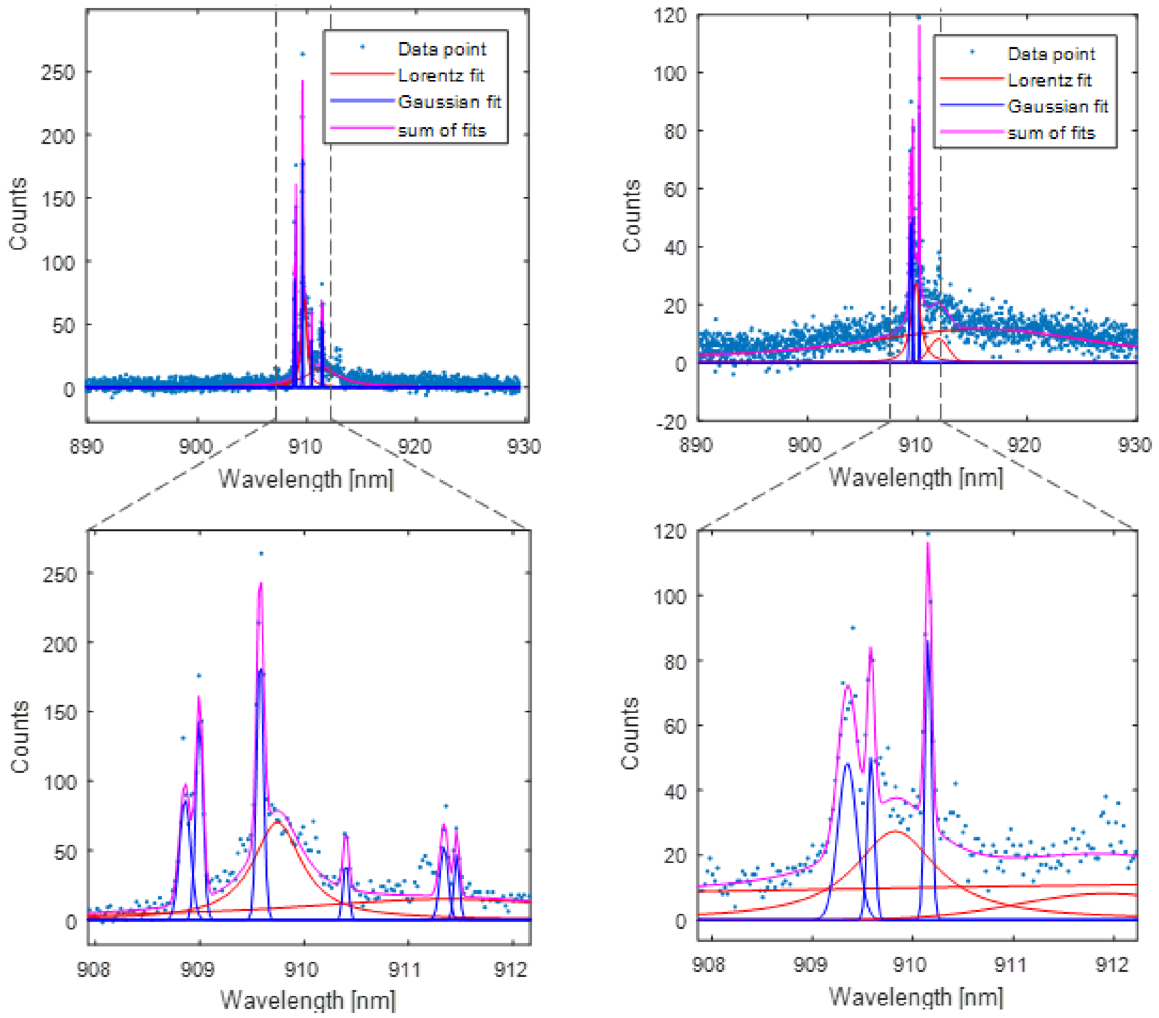

(a) (b)

FIGURE 6.3: Examples that implement a multi-fit to analyze photoluminescence spectra. (a) The multi-fit to PL spectra recorded at 6K. The solid red line shows the Lorentz fit applied to a cavity profile, while the solid blue line illustrates the Gaussian fit applied to QD emission profiles. The solid pink line represents the sum over all of the fits to data points (blue dots). A zoom-in figure that only shows the interesting region is exhibited in the bottom. (b) shows the same thing but at the temperature of 30.9K.

6.2.2 Power-dependence of cavity and QD

The photon-photon interaction is essential and needs to be exploited in many applications concerning quantum information processing [47]. Coupling a single QD strongly in the cavity can pave a way to the interaction based on photons via nonlinearity [48, 49]. The mechanism of nonlinearity in a QD is that a two-level system can only absorb one photon at a time. Therefore the incoming resonant two- or higher-photons can be transmitted partially, and the entanglement can be generated during the process [50]. The QD stays passive without any excitation.

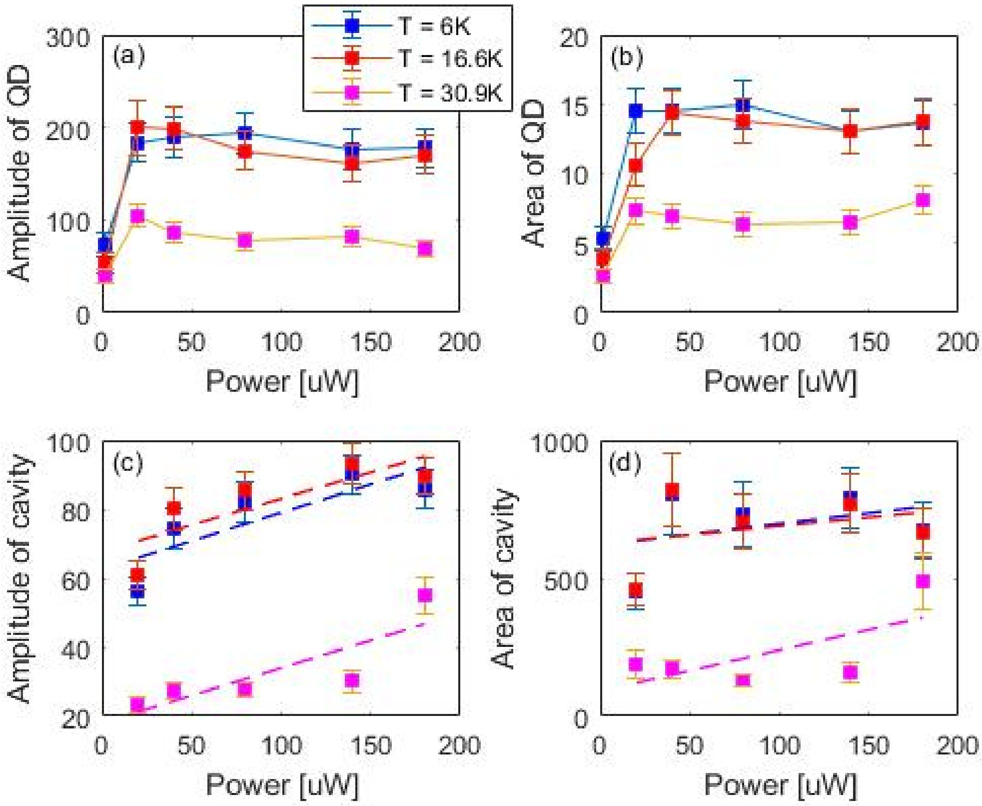

FIGURE 6.4: The response of QD and cavity to different excitation powers. (a) and (b) display the amplitude and area under Gaussian fit to QD emission, while (c) and (d) show the amplitude and area under Lorentz fit to cavity.

Figure 6.4 (a) and (b) show the saturation behavior for a single QD. Figure 6.4 (a) shows the max amplitude of the Gaussian peaks from the fitting of the QD spectra, and Figure 6.4 (b) presents the integrated area of the Gaussian peaks. It is clear that the QD saturates, and the saturation power should be between 2 μW and 20 μW. Unfortunately, there are no powers between that have been investigated. Hence the specific saturation power is not possible to be fit extracted.

In contrast, the cavity shows a linear relationship with the pumping power, that is, the more photons oscillated in the cavity leads to more energy restored. Figure 6.4 (c) and (d) show this linear dependence. Figure 6.4 (c) is the plot of amplitudes of Lorentz peaks from the fitting over the cavity, as a function of different input powers. Figure 6.4 (d) shows the integrated area of Lorentz peaks with different powers.

6.2.3 QD-tunning in cavity as a function of temperature

Information regarding the characteristics of the cavity and the coupled QD is extracted from the PL fitting and illustrated in Figure 6.5. It covers the data over six different temperatures between 6K and 30.9K. Figure 6.5 (a) shows the tuning of cavity resonance with the error bar, as a function of temperature. Overall, the cavity resonance is nearly unchanged with the temperature, and the majority is distributed around 909.69 nm. The cavity resonance under 30.9K has a considerable error due to the low count rate of the PL signal, as shown in Figure 6.5 (d). However, based on the simulation indicating the dependence of temperature to the cavity resonance, as shown in Figure 3.11, a shift of 0.15 nm is expected. The reasons for the low count rate are the unavoidable fitting error and the mismatched doping of GaAs during the growth process. For example, the detuning of self-assembled InAs QD embedded in GaAs structure, as reported in [51] and [52], also exhibit a different speed of detuning with increasing temperature. In contrast, the QD emission has a perfect tuning track with the temperature and an approximately 0.6 nm shift is achieved. For the data under the same temperature, but in different excitation powers, a good overlap is observed. We argue that the count rate of peaks in the PL spectra is the key factor influencing the quality of fitting. According to the information extracted from the cavity and QD, the detuning can be obtained as shown in Figure 6.5 (d). Overall, the detuning at different powers has a good consistency, and the extent of detuning is from roughly -0.2 nm to +0.4 nm. Figure 6.5 (d) shows the decrease of the amplitude of QD emission along with the increasing temperature. The brightness decreases slowly from 6K to 20K and rapidly above that. One reason could be, as investigated [53], the PL of QDs drops with the temperature increases. Another possibility is, the optimization of the count rate is insufficient after the tuning of temperature, as the sample could drift during the process.

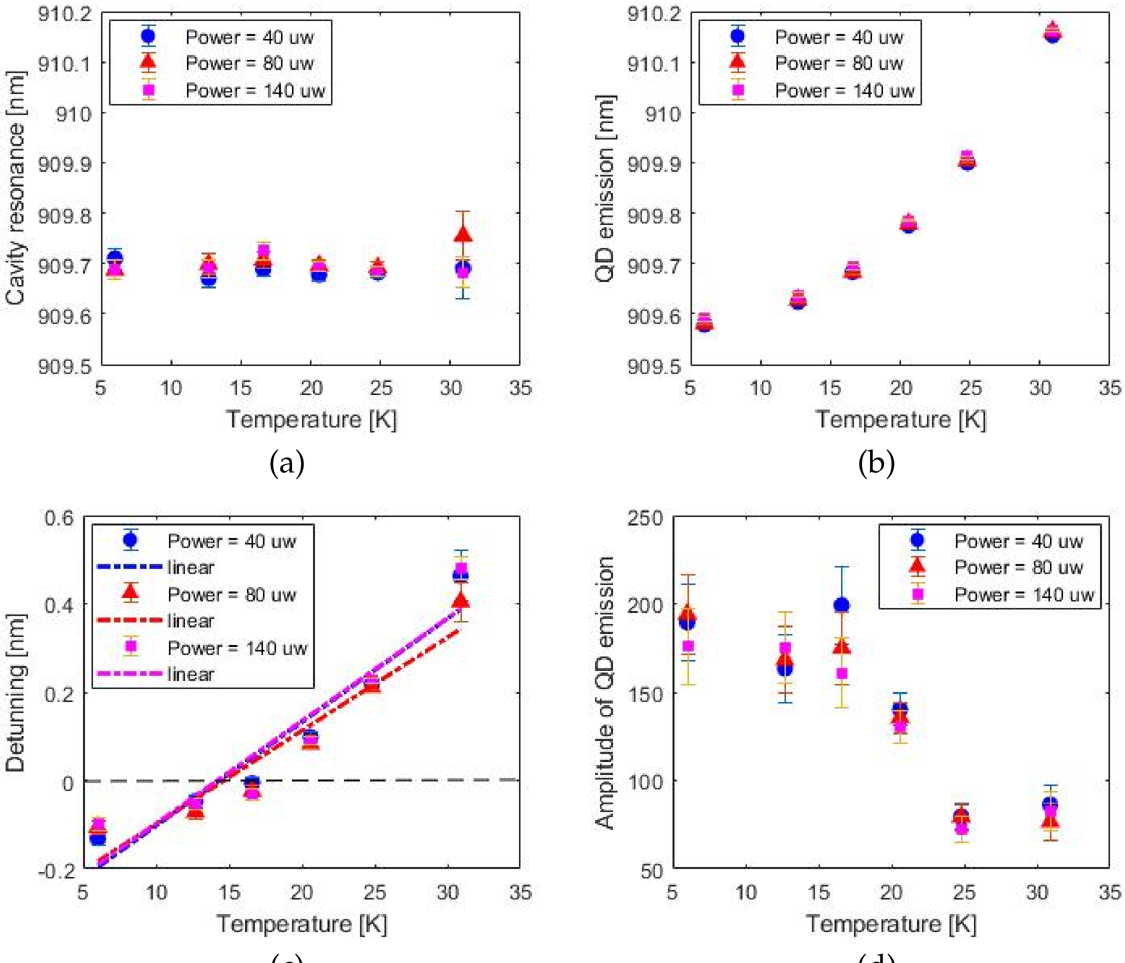

(a) (b)

(c) (d)

FIGURE 6.5: Temperature dependent information extracted from the PL fits. (a) The cavity resonance change is small varies temperatures from 6K to 30.9K. (b) The QD emission shifts at the temperatures varies from 6K to 30.9K. (c) The detuning of the QD to the cavity resonance at different temperatures. For each set of data, the linear guide to the eye is shown. (d) The amplitude of the Gaussian fit to the QD emission, under different temperatures. For all of the figures, three different excitation powers, $40\mu W$, $80\mu W$ and $140\mu W$, are performed.

6.3 Lifetime measurement

6.3.1 QD decay in bulk

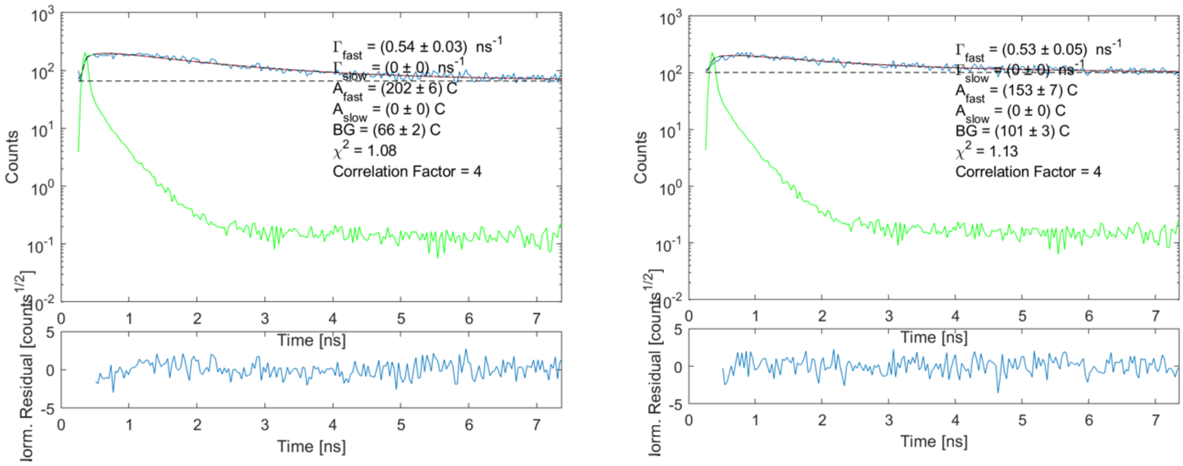

(a) (b)

FIGURE 6.6: PL decay of a QD in the bulk, measured with a non-resonant excitation scheme. (a) and (b) presents measures to two different QDs. For each of them, the top figure shows decay curves of QD (blue), the fit to decay data(red), and the IRF (green). The normalized residual of fitting is displayed at the bottom.

The lifetime of two typical QDs in the bulk area is measured and shown in Figure 6.6. The solid red line shows the single-exponential fit to the data, and the green line is the measured instrument response function (IRF); moreover, the normalized residual of the fitting as a function of time is shown at the bottom. There are three different QDs in total in the bulk that have been measured, but only 2 of them are presented here. The measured QDs are chosen based on the criterion that the position of QDs should be far away from the side wall. Due to the low count rate from the emission of QDs, the acquisition time is rather long (5 min), therefore the background counts (black dashed line) is high. One of the two QDs is measured with a decay rate of $0.54 \pm 0.03\ \mathrm{nm}^{-1}$, and another one is with decay rate of $0.53 \pm 0.05\ \mathrm{ns}^{-1}$. The third measured bulk QD which is not presented here has a fast decay rate of $0.54 \pm 0.04\ \mathrm{ns}^{-1}$. On average the three QD have a decay rate of $0.54 \pm 0.04\ \mathrm{ns}^{-1}$, corresponding to a lifetime of ~ 1.87 ns.

6.3.2 QD decay in cavity

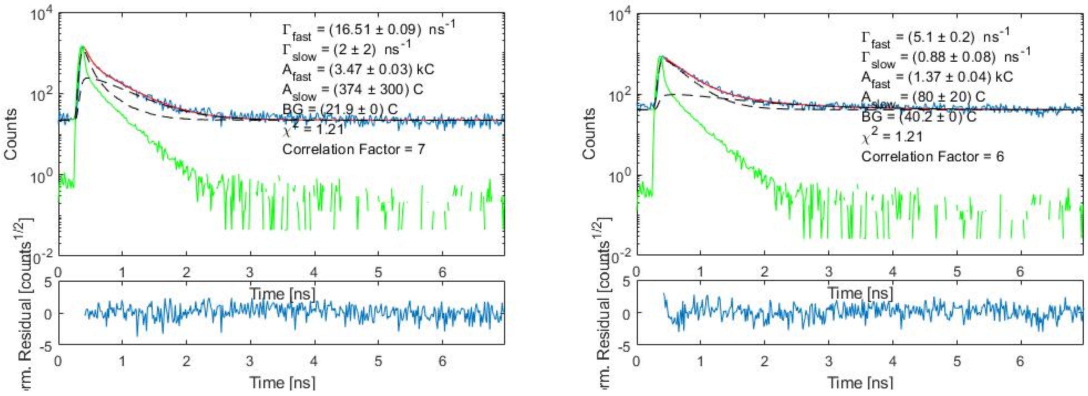

(a) (b)

FIGURE 6.7: PL decay of QD that is coupled in cavity, measured with a non-resonant excitation scheme. (a) and (b) presents measures at 6K and 30.9K, respectively. For each of them, the top figure shows decay curves of QD (blue), the fit to decay data(red), and the IRF (green). The normalized residual of fitting is displayed at the bottom.

The lifetime of QDs coupled with the cavity is presented in Figure 6.7. The (a) and (b) show the results at 6K and 30.9K, respectively. In contrast with the decay in bulk, the decay in the cavity is fitted with a bi-exponential function due to the co-existence of bright state and dark state, as introduced in section 2.2.1. The dark state exists in the QD coupled to a cavity and in the bulk QD, but the rate of the spin-flip process strongly depends on the distance from QD to the structure surface [11]. Therefore, the slow decay in the cavity cannot be ignored, whereas in the bulk the spin-flip process is negligible. For the measured decay under 6K, we measure a "fast" and a "slow" component, according to their relative decay rates. The fast component of decay rate is $16.51 \pm 0.09\ \text{ns}^{-1}$, corresponding to a lifetime of ~ 60.5 ps. The instrument response function (IRF) might be a limitation for the measurement, however, our fitting model only takes into consideration the data points. The fast decay rate of the coupled QD decreases to $5.1 \pm 0.2\ \text{ns}^{-1}$ at 30.9K, resulting a lifetime of ~ 196 ps. A comparison between the decay originated from the QD that is coupled in the cavity, on bulk material and the IRF is illustrated in Figure 6.8. This comparison shows that a cavity can significantly enhance the rate of fast decay and control the spontaneous emission of a QD coupled to it.

All of the decay data from different temperatures are fitted with the same set of parameters, to reflect the actual trend of temperature-dependent decays. The optimum set of the fitting parameter is achieved by examining whether it is in agreement with all of the decays with a minimally acceptable deviation. The deviation is assessed in terms of the correlation factor and χ^2 of fitting.

The decay rate here is measured under non-resonant excitation, and there might be a difference between the determined lifetime using resonant versus non-resonant excitation [46]. However, this sample is not based on a gated structure, which means that the QD emission line is broadened many times of its lifetime-limited linewidth. Hence the QD will not stay resonant with an incoming laser light, and a resonance excitation scheme cannot be easily performed on this sample.

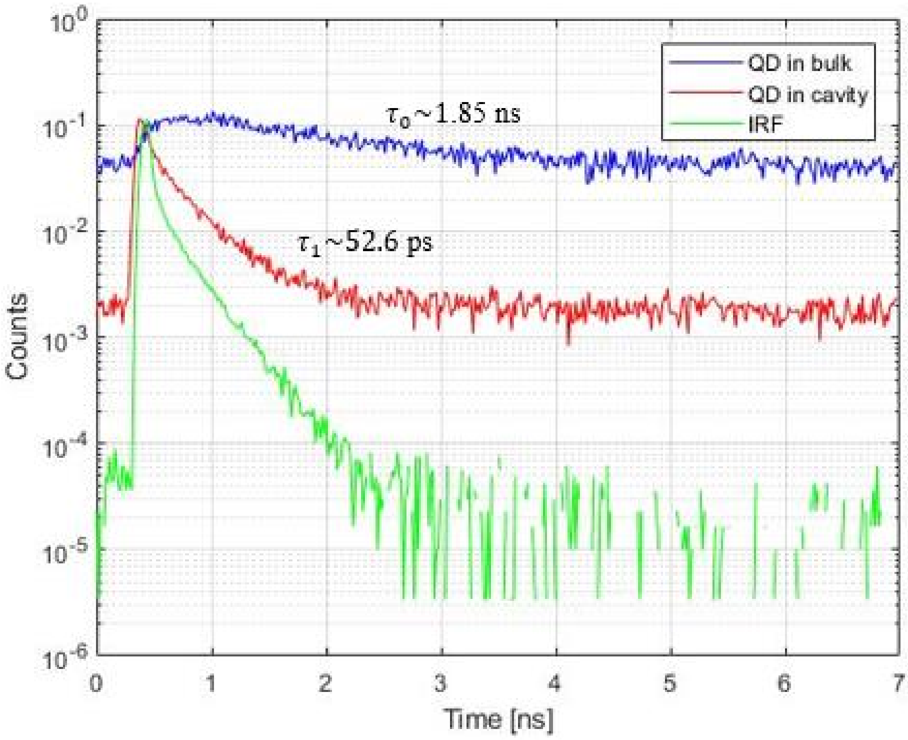

FIGURE 6.8: PL decays of QD located in bulk material (blue), coupled in the cavity (red) at 16.6K and the IRF (green).

6.3.3 Characterization of the decay dynamics

Figure 6.9 presents the plots of the fast component of decay, slow component of decay and also the ratio of them, as a function of wavelength, to characterize the decay dynamics at different temperatures and hence at different detunings to the cavity. By extracting the emission wavelength of the QD at different temperatures, the temperature-dependent decays can be converted to wavelength-dependent. Overall, the fast and slow component show the same temperature dependent trend, and it leads to a flat more or less constant ratio of the two. Specifically, the fast decay rises at the beginning, and reaches the highest value of $19 \pm 2\,\mathrm{ns}^{-1}$ at 909.67 nm, then drops until $5.1 \pm 0.2\,\mathrm{ns}^{-1}$ as it is being tuned away from the resonance. The slow decay originates from the non-radiative decay from the long-lived dark state. The slow decay follows a similar trend with the fast decay, but the determined rates are relatively high and not kept constant, compared to [11]. However, we argue that the slow decay is different from sample to sample, and the magnitude of slow decay depends on the size of the QD and the distance to the side wall. Another possibility is that the bright and dark excitons can be transferred between each other by the photon-mediated spin-flip process [11]. Hence the rate of spin-flip influences the overall exhibited slow decay rate. It may also occur that the mixing of transitions originating from neighboring coupled QDs during probing, this however, we assume to be a negligible effect.

The values of $\Gamma_{fast}/\Gamma_{slow}$ are mainly in between 5 and 10, according to this, we can speculate the possible area of this embedded QD, as the magenta color indicated in Figure 3.12 (c).

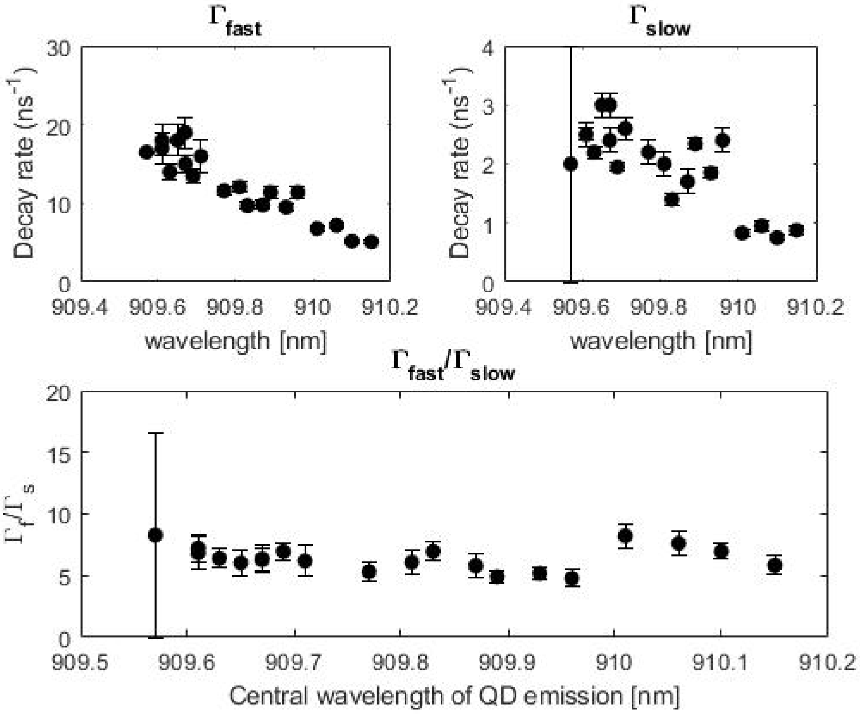

FIGURE 6.9: Plots of the fast component of decay rate, slow component of decay rate and the ratio between them, as a function of wavelength, for one cavity.

The fast and slow amplitude of decay contains the information regarding the LDOS of the modified environment and also the rate of the spin-flip process [11]. Figure 6.10 shows the fast and slow amplitude components of decays. The A_{fast} and A_{slow} exhibits the same varying trend with temperature and therefore with cavity detuning. The magnitude of amplitude depends on the number of QDs probed. Furthermore, the A_{fast} follows the trend of Γ_{fast} and the A_{fast} follows the trend of Γ_{fast}. The ratio between the fast and slow component of amplitude $A_{f/s}$ keeps approximately constant. The ratio is proportional to the LDOS and inversely proportional to the rate of the spin-flip process.

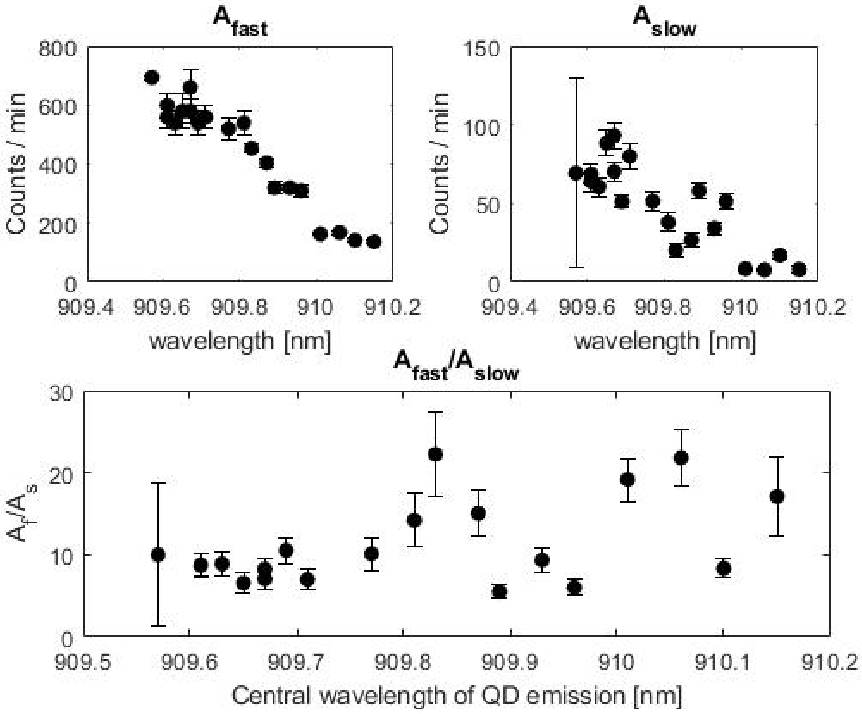

FIGURE 6.10: Plots of the fast component of amplitude, slow component of amplitude and the ratio between them, as a function of wavelength, for one cavity

6.4 Discussion of the PL and lifetime measurement results

The measurement results from the PL spectroscopy and lifetime measurement are compared to each other and shown in Figure. 6.11. The PL spectroscopy is employed to characterize the cavity resonance and the QD emission at different temperatures, and we have found the cavity resonance is almost unchanged at around 909.7nm, while the QD emission is shifted from 909.57nm to 910.15nm, leading to a detuning range between -0.2 nm to 0.4 nm, approximately. By plotting the fast component of the decay rate, as a function of wavelength, we can investigate whether the enhanced rate of spontaneous decay is caused by coupling to the cavity. In Figure 6.11, the cavity spectra fitted from the PL spectra at various temperatures is presented, and the decay rates at these specific temperatures are also plotted. The amplitude of cavities shows a dependence on temperature and the strength of coupling with the QD, which can be concluded from the fact that the strongest amplitude of cavity occurred at 16.6K and the weakest occurred at 30.9K. Overall, the majority of decays follows the cavity profile, and this strong correlation indicates that the significant enhancement to the decay rate is originated from the cavity.

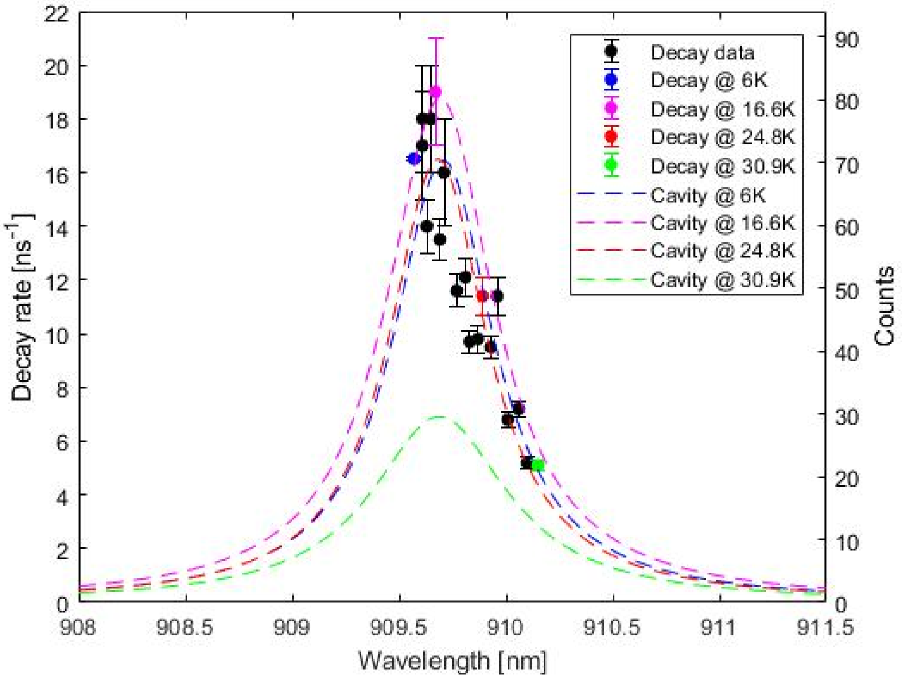

FIGURE 6.11: The comparison between PL and lifetime measurement. The black dotted lines present all of the cavities from PL after multi-fit, while blue dots with error bar exhibit the fast component of decay data from lifetime measurement.

Chapter 7

Conclusion and Outlook

In this project, we have investigated a light-matter interface, a novel GaAs-based nanobeam cavity, that enhance the emission from self-assembled InAs QD while at the same time can reduce the influence of charge noise on the QD optical transition frequency. The interface should not only provide a high intrinsic quality factor for the fundamental oscillating mode but also protect the QD from spectral diffusion originated from the etched defects. Hence a modulated outline has been applied to the cavity surface. The ability of the cavity to control the spontaneous emission of the coupled QD while providing a sufficient distance to etched surfaces was the focus of the project.

From simulation, the dispersion relation for a unit cell with a circular hole inside has been calculated, and the crucial information of band-edge wavelength is extracted to construct the cavity with a parabolic potential well in the extent of the cavity. Based on the calculated lattice constants for a "standard" narrow waveguide cavity, the width of the cavity is stretched to increase the distance to the surfaces. The lattice constants are optimized by conducting a parametric sweep. The parameters of the wide cavity are eventually determined by examining the quality factor and cavity resonance from the sweeping result. For the designed model, the quality factor can achieve 4.5×10^4 for 450nm wide cavity and 2.4×10^4 for 600nm wide cavity before full optimization of the cavity parameters. The wider cavity leads to a lower achievable intrinsic quality factor, which is expected due to the increasing scattering loss. Furthermore, the boundary holes located at the cavity center are investigated, and the multiple of enhancement (with an optimum radius of $\sim$28nm) to the quality factor is ~ 2.2 for 450nm wide cavity and ~ 2.5 for 600nm wide cavity. In the end, the intrinsic Q can reach 10^5 for 450nm cavity and 6×10^4 for the 600nm cavity. Moreover, the transmission spectrum at cavity resonance reveals a blue-shift in resonance wavelength as the increasing number of loaded mirror holes, and so does the transmittance as a function of the number of mirrors.

For the experimental part, the 450 nm-wide cavity has been fabricated and measured. From the calculated transmittance, we estimate reasonable fabrication parameters, such that the number of coupled mirror holes should be less than three to achieve above 90% transmission. At room temperature, we characterized the quality factors and cavity resonances for 60 cavities. The quality factor is distributed in the range of 300∼1200 and shows a correlation with the number of mirrors. At cryogenic temperature, the strong coupling of a QD to a cavity is observed. The PL spectroscopy in combination with the temperature tuning is conducted to modify the spectral matching between QD emission and cavity mode. The QD emission is tuned from 909.57nm to 910.15nm, over a temperature range of 6∼30.9K, while the cavity resonance is nearly unchanged at ∼909.7nm. By measuring the lifetime as a function of temperature, the highest fast decay rate of 19±2 ns^{-1} is achieved and corresponds to a Purcell factor of ∼36 under a non-resonant excitation scheme.

Some improvements and further investigations may be implemented for this project. First, the wide cavity is essentially an L2 cavity confining the dielectric mode. The L3 cavity which modulates the air mode would be a choice to try. However, it may also bring more bulk area in the cavity center by taking out more holes. In the experimental part, the single-photon source could perform better by using a gated structure, and it would also enable the investigation of the nonlinear optics [54]. To achieve coupling of cavity with a single QD, a low QD density wafer could be used for fabrication, yet it still needs an improved fabrication technique to position the QDs [55]. The shallow-etched grating coupler may also be employed for a much higher extraction efficiency [56].

The ultimate vision would be the construction of a scalable photonic quantum network, to enable an advanced quantum information processing and transferring. In this network, the stationary positioned QDs can be connected by flying qubits represented by single photons [57]. This project has discussed the nanobeam cavity that is able to strongly couple and enhance the QD emission, thus could contribute to the realization of an effective single-photon source. Connecting the stationary nodes (QDs) by flying qubit (single photons) would open up a window for such a network [12], and Figure 7.1 illustrates the necessary basic puzzles towards this goal. The increasing development of semiconductor photonic integrated circuits also exhibits the possibility to integrate all of the functionalities into one single photonic chip. The QD-photonic nanostructure-based quantum network shows enormous potential, and we look forward to more remarkable progress in the near future.

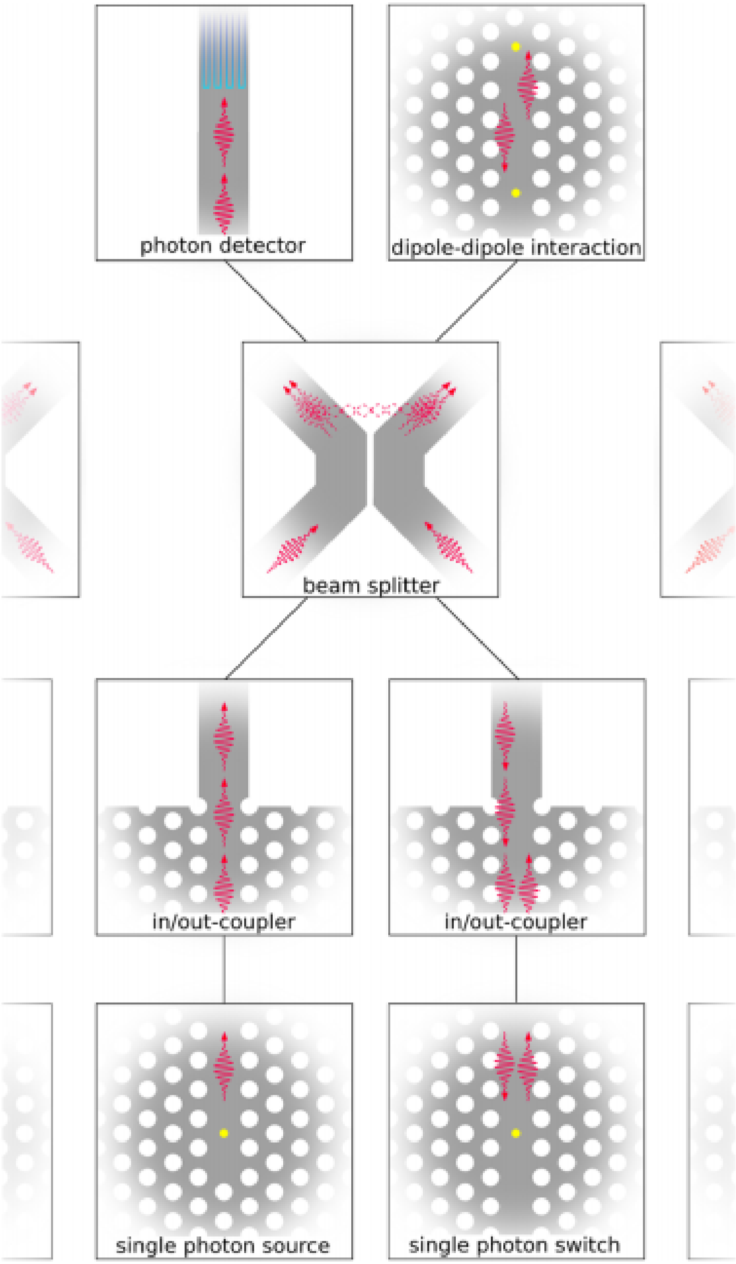

FIGURE 7.1: The basic puzzles for constructing a photonic quantum network. The puzzles should include the single-photon sources or a switch to generate the train of single photons, and a highly efficient in/out coupler should be employed to extract single photons. For the processing unit, a beam splitter can provide a path-entanglement. A superconducting single photon detector can be registered to conduct a precisely measurement. Multiple QDs can be controlled and coupled by dipole-dipole interaction in a waveguide. Figure from [12]

Appendix A

Appendix

A.1 More fitting result from PL measurement results

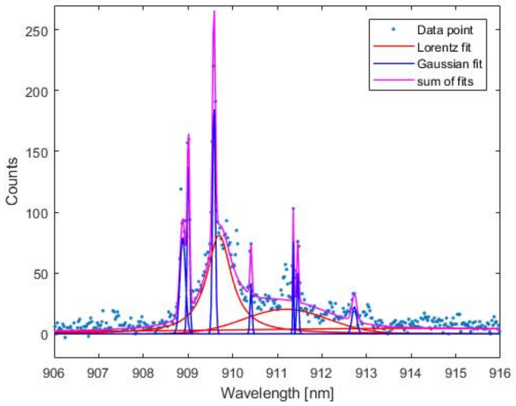

6K @ 80μW

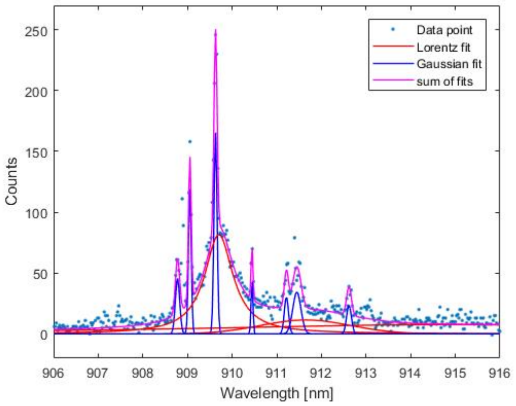

12.7K @ 80μW

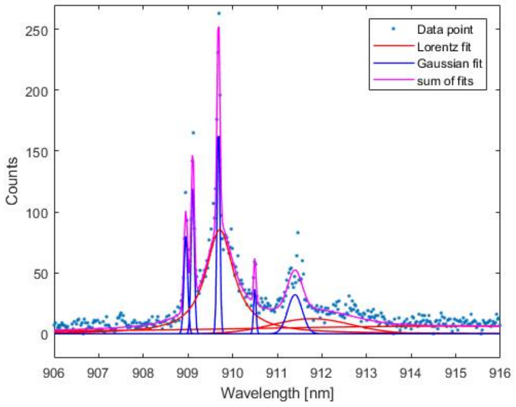

16.6K @ 80μW

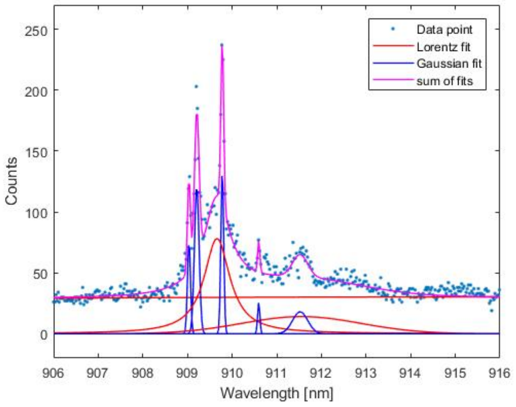

20.6K @ 80μW

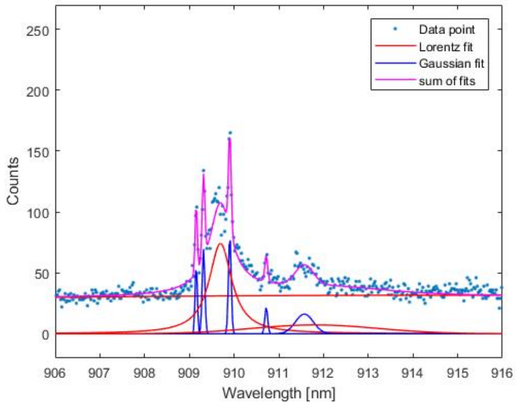

24.8K @ 80μW

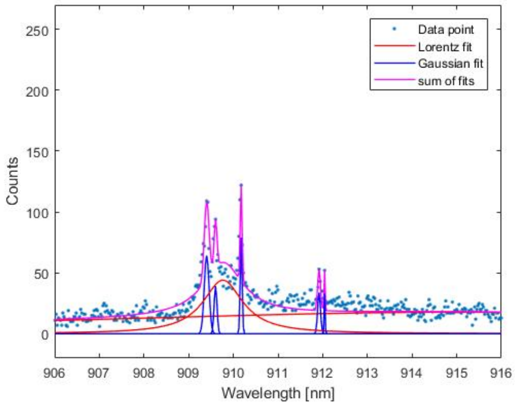

30.9K @ 80μW

A.2 More fitting result from lifetime measurement results

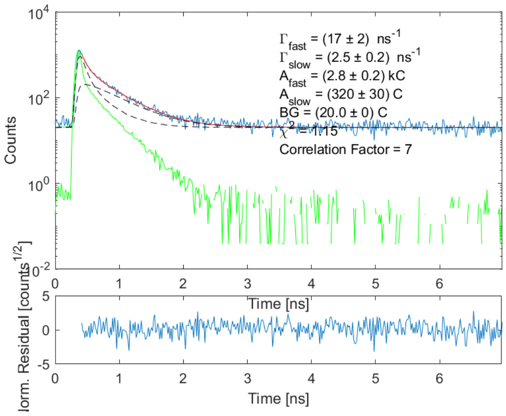

8.9K

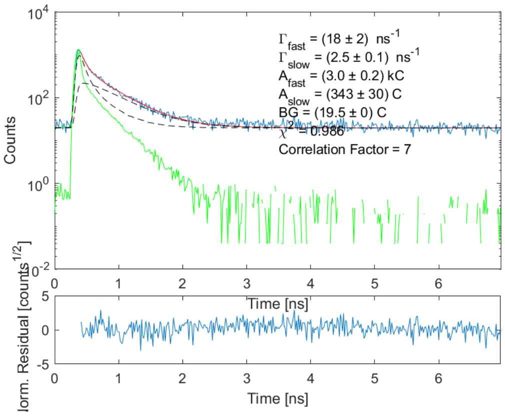

10.8K

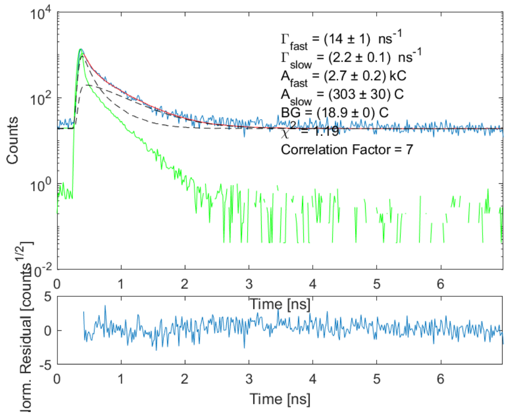

12.7K

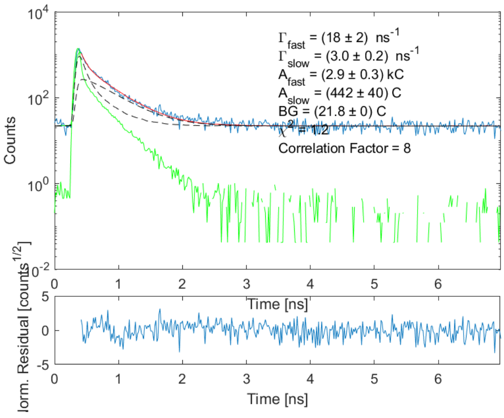

14.7K

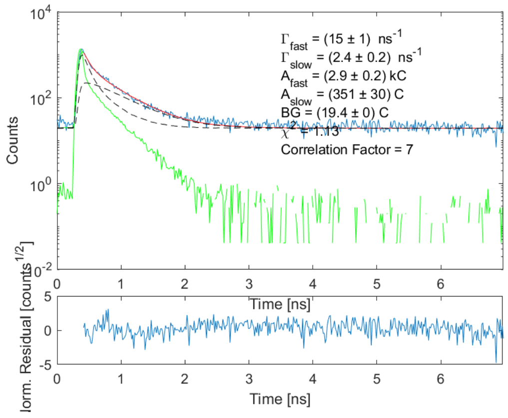

15.7K

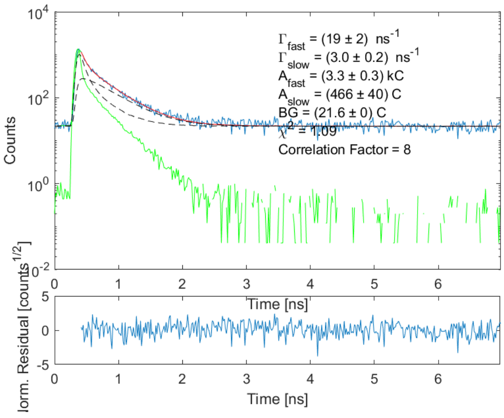

16.6K

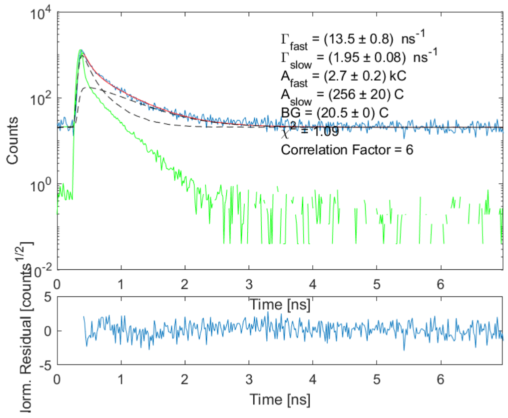

17.6K

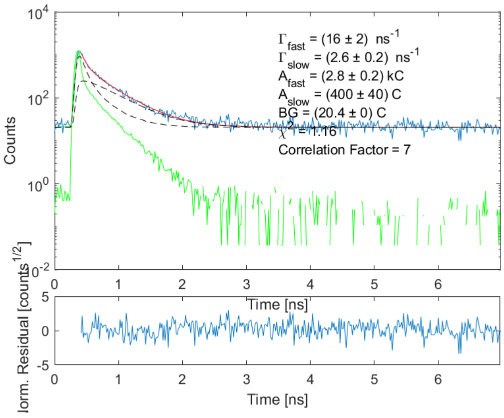

18.6K

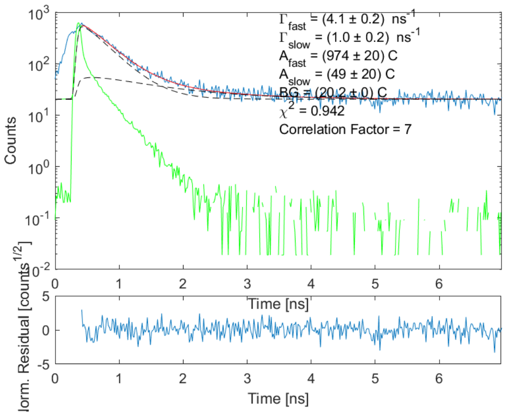

19.6K

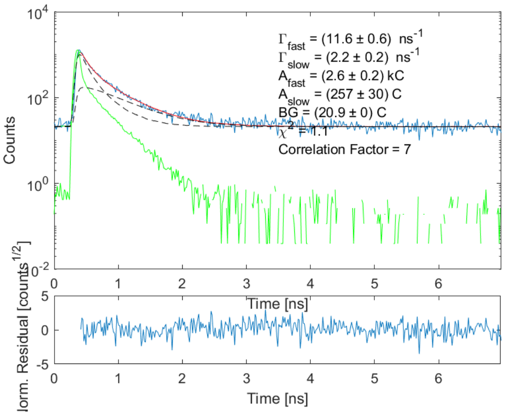

20.7K

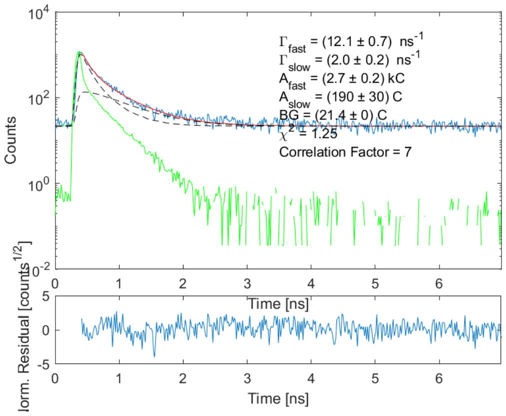

21.7K

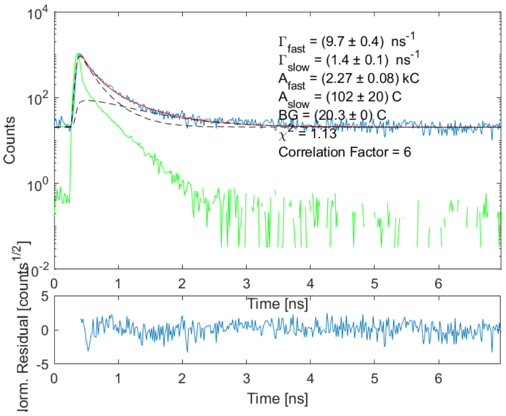

22.7K

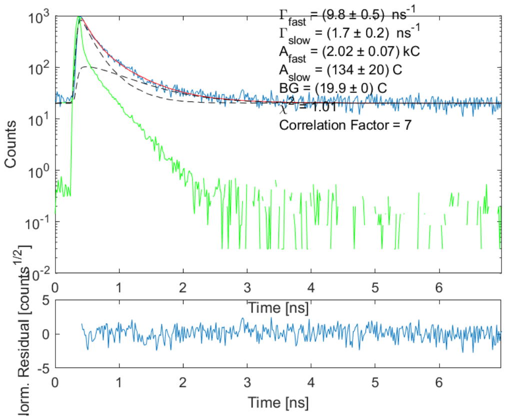

23.7K

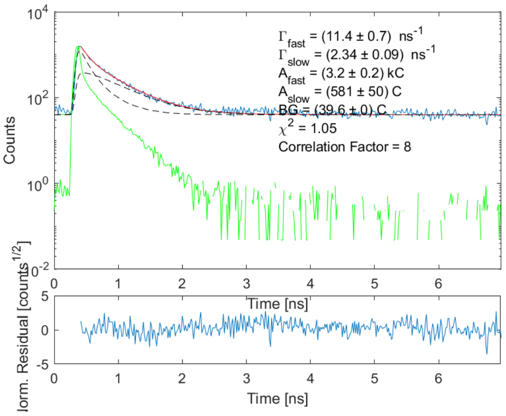

24.8K

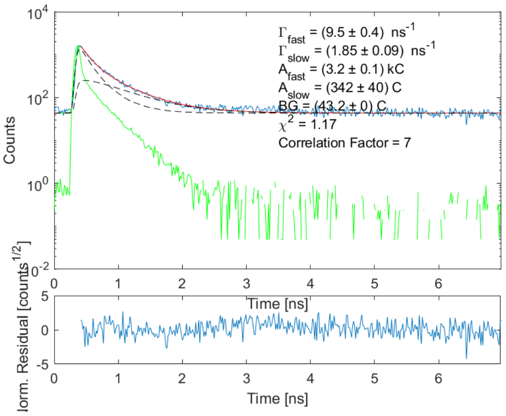

25.7K

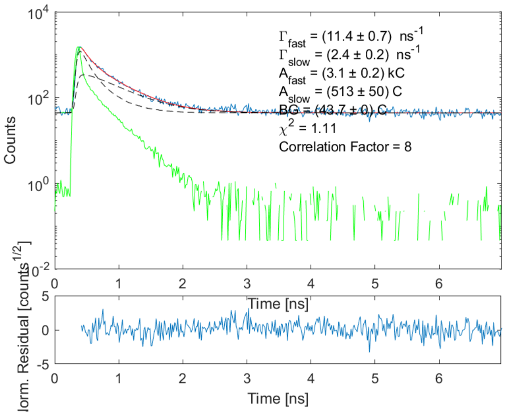

26.8K

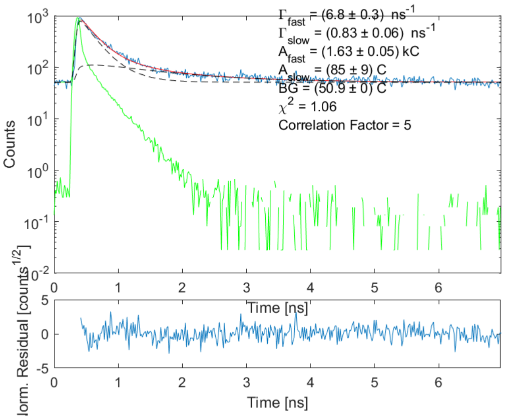

27.9K

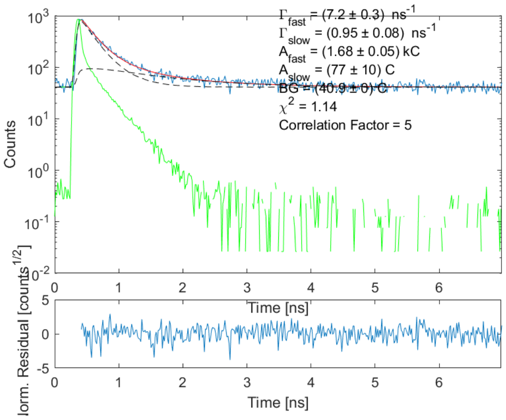

28.9K

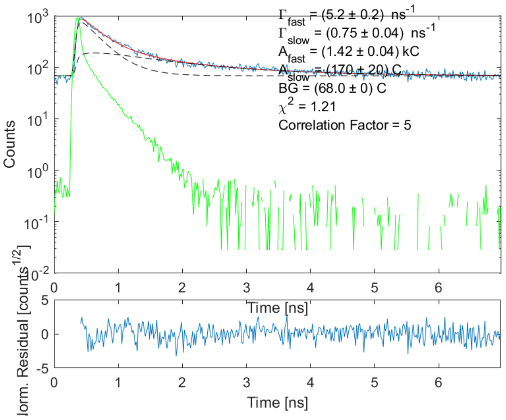

29.9K

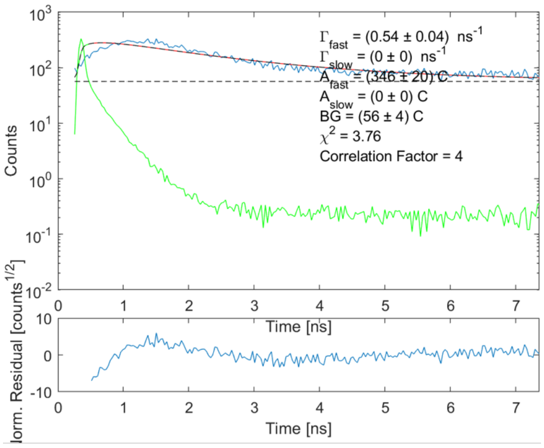

Bulk 3

Bibliography

[1] J. Liu, K. Konthasinghe, M. Davanço, J. Lawall, V. Anant, V. Verma, R. Mirin, S. W. Nam, J. D. Song, B. Ma, *et al.*, "Single self-assembled inas/gaas quantum dots in photonic nanostructures: The role of nanofabrication," *Physical Review Applied*, vol. 9, no. 6, p. 064019, 2018.

[2] H. Thyrrestrup, G. Kirsanske, H. Le Jeannic, T. Pregnolato, L. Zhai, L. Raahauge, L. Midolo, N. Rotenberg, A. Javadi, R. Schott, *et al.*, "Quantum optics with near-lifetime-limited quantum-dot transitions in a nanophotonic waveguide," *Nano letters*, vol. 18, no. 3, pp. 1801–1806, 2018.

[3] S.-K. Liao, W.-Q. Cai, W.-Y. Liu, L. Zhang, Y. Li, J.-G. Ren, J. Yin, Q. Shen, Y. Cao, Z.-P. Li, *et al.*, "Satellite-to-ground quantum key distribution," *Nature*, vol. 549, no. 7670, p. 43, 2017.

[4] J.-G. Ren, P. Xu, H.-L. Yong, L. Zhang, S.-K. Liao, J. Yin, W.-Y. Liu, W.-Q. Cai, M. Yang, L. Li, *et al.*, "Ground-to-satellite quantum teleportation," *Nature*, vol. 549, no. 7670, p. 70, 2017.

[5] B. Lounis and M. Orrit, "Single-photon sources," *Reports on Progress in Physics*, vol. 68, no. 5, p. 1129, 2005.

[6] N. Somaschi, V. Giesz, L. De Santis, J. Loredo, M. P. Almeida, G. Hornecker, S. L. Portalupi, T. Grange, C. Antón, J. Demory, *et al.*, "Near-optimal single-photon sources in the solid state," *Nature Photonics*, vol. 10, no. 5, p. 340, 2016.

[7] D. Huber, M. Reindl, Y. Huo, H. Huang, J. S. Wildmann, O. G. Schmidt, A. Rastelli, and R. Trotta, "Highly indistinguishable and strongly entangled photons from symmetric gaas quantum dots," *Nature communications*, vol. 8, p. 15506, 2017.

[8] J. Liu, K. Konthasinghe, M. Davanco, J. Lawall, V. Anant, V. Verma, R. Mirin, S. W. Nam, J. D. Song, B. Ma, *et al.*, "Direct observation of nanofabrication influence on the optical properties of single self-assembled inas/gaas quantum dots," *arXiv preprint arXiv:1710.09667*, 2017.

[9] J. Márquez, L. Geelhaar, and K. Jacobi, "Atomically resolved structure of inas quantum dots," *Applied Physics Letters*, vol. 78, no. 16, pp. 2309–2311, 2001.

[10] M. Bayer, G. Ortner, O. Stern, A. Kuther, A. Gorbunov, A. Forchel, P. Hawrylak, S. Fafard, K. Hinzer, T. Reinecke, *et al.*, "Fine structure of neutral and charged excitons in self-assembled in (ga) as/(al) gaas quantum dots," *Physical Review B*, vol. 65, no. 19, p. 195315, 2002.

[11] J. Johansen, B. Julsgaard, S. Stobbe, J. M. Hvam, and P. Lodahl, "Probing long-lived dark excitons in self-assembled quantum dots," *Physical Review B*, vol. 81, no. 8, p. 081304, 2010.

[12] P. Lodahl, S. Mahmoodian, and S. Stobbe, "Interfacing single photons and single quantum dots with photonic nanostructures," *Reviews of Modern Physics*, vol. 87, no. 2, p. 347, 2015.

[13] P. Senellart, G. Solomon, and A. White, "High-performance semiconductor quantum-dot single-photon sources," *Nature nanotechnology*, vol. 12, no. 11, p. 1026, 2017.

[14] G. Brassard, N. Lütkenhaus, T. Mor, and B. C. Sanders, "Limitations on practical quantum cryptography," *Physical Review Letters*, vol. 85, no. 6, p. 1330, 2000.

[15] N. Spagnolo, C. Vitelli, M. Bentivegna, D. J. Brod, A. Crespi, F. Flamini, S. Giacomini, G. Milani, R. Ramponi, P. Mataloni, *et al.*, "Experimental validation of photonic boson sampling," *Nature Photonics*, vol. 8, no. 8, p. 615, 2014.

[16] J. B. Spring, B. J. Metcalf, P. C. Humphreys, W. S. Kolthammer, X.-M. Jin, M. Barbieri, A. Datta, N. Thomas-Peter, N. K. Langford, D. Kundys, *et al.*, "Boson sampling on a photonic chip," *Science*, vol. 339, no. 6121, pp. 798–801, 2013.

[17] M. A. Broome, A. Fedrizzi, S. Rahimi-Keshari, J. Dove, S. Aaronson, T. C. Ralph, and A. G. White, "Photonic boson sampling in a tunable circuit," *Science*, vol. 339, no. 6121, pp. 794–798, 2013.

[18] C.-K. Hong, Z.-Y. Ou, and L. Mandel, "Measurement of subpicosecond time intervals between two photons by interference," *Physical review letters*, vol. 59, no. 18, p. 2044, 1987.

[19] J. D. Joannopoulos, S. G. Johnson, J. N. Winn, and R. D. Meade, *Photonic crystals: molding the flow of light*. Princeton university press, 2011.

[20] J. H. Davies, *The physics of low-dimensional semiconductors: an introduction*. Cambridge university press, 1998.

[21] S. G. Johnson and J. D. Joannopoulos, "Introduction to photonic crystals: Bloch's theorem, band diagrams, and gaps (but no defects)," *Photonic Crystal Tutorial*, pp. 1–16, 2003.

[22] L. Novotny and B. Hecht, *Principles of nano-optics*. Cambridge university press, 2012.

[23] Y. Yamamoto and A. Imamoglu, "Mesoscopic quantum optics," *Mesoscopic Quantum Optics, published by John Wiley & Sons, Inc., New York, 1999.*, 1999.

[24] P. Lodahl, A. F. Van Driel, I. S. Nikolaev, A. Irman, K. Overgaag, D. Vanmaekelbergh, and W. L. Vos, "Controlling the dynamics of spontaneous emission from quantum dots by photonic crystals," *Nature*, vol. 430, no. 7000, p. 654, 2004.

[25] P. Yao, V. Manga Rao, and S. Hughes, "On-chip single photon sources using planar photonic crystals and single quantum dots," *Laser & Photonics Reviews*, vol. 4, no. 4, pp. 499–516, 2010.

[26] N. Ha, T. Mano, Y.-L. Chou, Y.-N. Wu, S.-J. Cheng, J. Bocquel, P. M. Koenraad, A. Ohtake, Y. Sakuma, K. Sakoda, *et al.*, "Size-dependent line broadening in the emission spectra of single gaas quantum dots: Impact of surface charge on spectral diffusion," *Physical Review B*, vol. 92, no. 7, p. 075306, 2015.

[27] S. Empedocles, D. Norris, and M. Bawendi, "Photoluminescence spectroscopy of single cdse nanocrystallite quantum dots.," *Physical Review Letters*, vol. 77, no. 18, pp. 3873 – 3876, 1996.

[28] S. A. Blanton, M. A. Hines, and P. Guyot-Sionnest, "Photoluminescence wandering in single cdse nanocrystals," *Applied Physics Letters*, vol. 69, no. 25, pp. 3905–3907, 1996.

[29] J. Seufert, R. Weigand, G. Bacher, T. Kümmell, A. Forchel, K. Leonardi, and D. Hommel, "Spectral diffusion of the exciton transition in a single self-organized quantum dot," *Applied Physics Letters*, vol. 76, no. 14, pp. 1872–1874, 2000.

[30] V. Türck, S. Rodt, O. Stier, R. Heitz, R. Engelhardt, U. Pohl, D. Bimberg, and R. Steingrüber, "Effect of random field fluctuations on excitonic transitions of individual cdse quantum dots," *Physical Review B*, vol. 61, no. 15, p. 9944, 2000.

[31] R. Heitz, T. Ramachandran, A. Kalburge, Q. Xie, I. Mukhametzhanov, P. Chen, and A. Madhukar, "Observation of reentrant 2d to 3d morphology

transition in highly strained epitaxy: Inas on gaas," *Physical review letters*, vol. 78, no. 21, p. 4071, 1997.

[32] H. Robinson and B. Goldberg, "Light-induced spectral diffusion in single self-assembled quantum dots," *Physical Review B*, vol. 61, no. 8, p. R5086, 2000.

[33] C. Wang, A. Badolato, I. Wilson-Rae, P. Petroff, E. Hu, J. Urayama, and A. Imamoğlu, "Optical properties of single inas quantum dots in close proximity to surfaces," *Applied physics letters*, vol. 85, no. 16, pp. 3423–3425, 2004.

[34] A. Majumdar, E. D. Kim, and J. Vučković, "Effect of photogenerated carriers on the spectral diffusion of a quantum dot coupled to a photonic crystal cavity," *Physical Review B*, vol. 84, no. 19, p. 195304, 2011.

[35] T. Wood, C. Burrus, D. Miller, D. Chemla, T. Damen, A. Gossard, and W. Wiegmann, "High-speed optical modulation with gaas/gaalas quantum wells in ap-i-n diode structure," *Applied Physics Letters*, vol. 44, no. 1, pp. 16–18, 1984.

[36] R. Kubo, "A stochastic theory of line shape," *Advances in Chemical Physics: Stochastic Processes in Chemical Physics*, pp. 101–127, 1969.

[37] A. M. Ivinskaya, A. V. Lavrinenko, and D. M. Shyroki, "Modeling of nanophotonic resonators with the finite-difference frequency-domain method," *IEEE Transactions on Antennas and Propagation*, vol. 59, no. 11, pp. 4155–4161, 2011.

[38] Q. Quan, P. B. Deotare, and M. Loncar, "Photonic crystal nanobeam cavity strongly coupled to the feeding waveguide," *Applied Physics Letters*, vol. 96, no. 20, p. 203102, 2010.

[39] S. Hu, M. Khater, R. Salas-Montiel, E. Kratschmer, S. Engelmann, W. M. Green, and S. M. Weiss, "Experimental realization of deep-subwavelength confinement in dielectric optical resonators," *Science advances*, vol. 4, no. 8, p. eaat2355, 2018.

[40] C. Sauvan, G. Lecamp, P. Lalanne, and J.-P. Hugonin, "Modal-reflectivity enhancement by geometry tuning in photonic crystal microcavities," *Optics Express*, vol. 13, no. 1, pp. 245–255, 2005.

[41] A. Chalcraft, S. Lam, D. O'Brien, T. Krauss, M. Sahin, D. Szymanski, D. Sanvitto, R. Oulton, M. Skolnick, A. Fox, *et al.*, "Mode structure of the l 3 photonic crystal cavity," *Applied physics letters*, vol. 90, no. 24, p. 241117, 2007.

[42] P. B. Deotare, M. W. McCutcheon, I. W. Frank, M. Khan, and M. Lončar, “High quality factor photonic crystal nanobeam cavities,” *Applied Physics Letters*, vol. 94, no. 12, p. 121106, 2009.

[43] C. Sauvan, J.-P. Hugonin, I. Maksymov, and P. Lalanne, “Theory of the spontaneous optical emission of nanosize photonic and plasmon resonators,” *Physical Review Letters*, vol. 110, no. 23, p. 237401, 2013.

[44] M. N. Polyanskiy, “Refractive index database.” `https://refractiveindex.info`. Accessed on 2019-01-19.

[45] M. C. Teich and B. E. A. Saleh, *Fundamentals of Photonics (Wiley Series in Pure and Applied Optics).* John Wiley Sons Incorporated, n.d.

[46] F. Liu, A. J. Brash, J. O’Hara, L. M. Martins, C. L. Phillips, R. J. Coles, B. Royall, E. Clarke, C. Bentham, N. Prtljaga, *et al.*, “High purcell factor generation of indistinguishable on-chip single photons,” *Nature nanotechnology*, vol. 13, no. 9, p. 835, 2018.

[47] P. Lodahl, “Quantum-dot based photonic quantum networks,” *Quantum Science and Technology*, vol. 3, no. 1, p. 013001, 2017.

[48] A. Faraon, I. Fushman, D. Englund, N. Stoltz, P. Petroff, and J. Vučković, “Coherent generation of non-classical light on a chip via photon-induced tunnelling and blockade,” *Nature Physics*, vol. 4, no. 11, p. 859, 2008.

[49] A. Reinhard, T. Volz, M. Winger, A. Badolato, K. J. Hennessy, E. L. Hu, and A. Imamoğlu, “Strongly correlated photons on a chip,” *Nature Photonics*, vol. 6, no. 2, p. 93, 2012.

[50] D. Witthaut, M. D. Lukin, and A. S. Sørensen, “Photon sorters and qnd detectors using single photon emitters,” *EPL (Europhysics Letters)*, vol. 97, no. 5, p. 50007, 2012.

[51] D. Englund, A. Faraon, I. Fushman, N. Stoltz, P. Petroff, and J. Vučković, “Controlling cavity reflectivity with a single quantum dot,” *Nature*, vol. 450, no. 7171, p. 857, 2007.

[52] R. Bose, D. Sridharan, G. Solomon, and E. Waks, “Large optical stark shifts in semiconductor quantum dots coupled to photonic crystal cavities,” *Applied Physics Letters*, vol. 98, no. 12, p. 121109, 2011.

[53] D. Sreenivasan, J. Haverkort, H. Zhan, T. Eijkemans, R. Nötzel, and J. Wolter, “Photoluminescence study of low-temperature grown inas/gaas quantum dots.,” in *Proceedings of the 7th International Conference on Optoelectronics, Fiber*

Optics and Photonics: Photonics 2004 Conference, 9-11 December 2004, Cochin, India, 2004.

[54] A. Javadi, I. Söllner, M. Arcari, S. L. Hansen, L. Midolo, S. Mahmoodian, G. Kiršanskė, T. Pregnolato, E. Lee, J. Song, *et al.*, "Single-photon non-linear optics with a quantum dot in a waveguide," *Nature communications*, vol. 6, p. 8655, 2015.

[55] T. Pregnolato *et.al.*, in preparation (2019).

[56] X. Zhou, I. Kulkova, T. Lund-Hansen, S. L. Hansen, P. Lodahl, and L. Midolo, "High-efficiency shallow-etched grating on gaas membranes for quantum photonic applications," *Applied Physics Letters*, vol. 113, no. 25, p. 251103, 2018.

[57] W. Gao, P. Fallahi, E. Togan, A. Delteil, Y. Chin, J. Miguel-Sanchez, and A. Imamoğlu, "Quantum teleportation from a propagating photon to a solid-state spin qubit," *Nature communications*, vol. 4, p. 2744, 2013.